Stability and Quench Protection of High-Temperature Superconductors

by

Ing Chea Ang

B.S. in Mechanical Engineering
B.A. Mathematics-Economics
Lafayette College, 2004

Submitted to the Department of Mechanical Engineering in partial
fulfillment of the requirements for the degree of

Master of Science

at the

MASSACHUSETTS INSTITUTE OF TECHNOLOGY

June 2006

Author ______________________________
Department of Mechanical Engineering
May 12, 2006

Certified by ______________________________
Yukikazu Iwasa
Senior Lecturer, Dept. of Mechanical Engineering
Thesis Supervisor

Accepted by ______________________________
Lallit Anand
Chairman, Departmental Graduate Committee

Stability and Quench Protection of HTS Magnets

by

Ing Chea Ang

Submitted to the Department of Mechanical Engineering
on May 12, 2006 in partial fulfillment
of the requirements for the degree of
Master of Science

Abstract

In the design and operation of a superconducting magnet, stability and protection are two key issues that determine the magnet's reliability and safe operation. Although the high-temperature superconductor (HTS) is considered much more stable than the low-temperature superconductor (LTS), it is susceptible to damage caused primarily by three events that can occur in large-scale "real" devices: 1) overheating; 2) high voltage; and, 3) overstressing. In this thesis, we have investigated the first two issues as well acoustic emission (AE) technique as a possible mean for an early detection of a quench. For most of the experimental work reported here, we used "pancake" coils wound with coated YBCO conductor, the HTS of choice by those currently developing HTS-based electric power devices, though, YBCO itself to date is still in the development phase.

For protection against overheating, an HTS magnet assembled with pancake coils may be made self-protecting through speedy 2-D or even 3-D normal zone propagation (NZP) within its winding, aided by good thermally-diffusive turn-to-turn spacers. We have found experimentally that good thermal diffusivity alone, however, does not guarantee fast 2-D NZP: thermal contact resistance between winding layers plays a crucial role in NZP in the transverse direction. For high internal voltage, a small test "magnet" consisting of two pancake coils was studied to investigate the internal voltage distributions within the magnet when one of the pancakes was driven normal with a heater. Measured voltage distributions were compared with those of simulation. Finally, to complement standard resistive voltage technique, an acoustic emission (AE) technique was investigated for detection of a quench at an instance earlier than that possible with a resistive voltage technique. With improved understanding of these issues, we should be able to develop protection techniques that ensure reliable and safe operation of HTS devices.

Thesis Supervisor: Dr. Yukikazu Iwasa
Title: Head, Magnet Technology Division and Research Professor, Francis Bitter Magnet Laboratory, MIT;
Senior Lecturer, Department of Mechanical Engineering, MIT

Acknowledgement

This thesis work marks an important milestone in my intellectual exploration of the exciting world of science, where imagination meets reality and the impossible become possible. However, my experience would not have been made complete without the many professors, colleagues and friends who have so patiently assisted me along the way. In particular, my appreciation goes to my thesis supervisor, Dr. Yukikazu Iwasa, for his guidance, and instruction. He has shown me the art of good problem solving, for which he is the consummate artist. In addition, I would also like to thank post-doctorate associate, Frederic Trillaud, for his willingness to impart to me his expertise in stability and protection. Without him, this thesis work would be less than half-baked and my understanding of the French culture would have suffered drastically. I would also like to thank many others who worked in the lab the two years I have been there; Seung-yong Hahn for graciously guiding me when I was desperately lost, Haigun Lee for selflessly assisting me in my experiments, Juan Bascunan for the many coffee jokes that lightened my day, David Johnson for his technical assistance, and also every member of the Advanced Magnet Technology Division for giving me suggestions to improve my work. Special thanks also goes to John Voccio from American Superconductor Corporation for being such a pleasure to work with.

Lastly, there can be no words to express my gratitude for my family who has shown me so much love and support throughout my entire life. I thank my parents for giving me the ambition to achieve, the strength to succeed and the courage to attain my dreams. I am indeed blessed beyond measure to be a part of this wonderful family.

This thesis project was supported in part by the Air Force Office of Scientific Research.
Tape samples were provided by American Superconductor Corporation (Westborough, MA) and Hyper Tech Research Incorporated (Columbus, OH).
Diamond samples were provided by Tai-Yang Research (Knoxville, TN).

Table of Contents

List of Figures

List of Tables

Chapter 1- Introduction

1.1 Brief History

Even after 95 years since its discovery, superconductivity still never ceases to inspire the imagination. The discovery of superconductivity, which is the phenomenon of zero electrical resistance of certain materials at low temperature, was first discovered by Heike Kamerlingh Onnes in 1911, in the metal mercury at liquefied helium temperatures (4.2K). Thereafter, much research has been conducted to study this highly intriguing subject. For the most part of the 20th century, low temperature superconductors (LTS) were used to develop electrical devices. LTS is composed of metal compounds with critical temperatures below 20K. It was not until the late 1980's that oxide-based high-temperature superconductors (HTS) were discovered. These superconductors operated at high critical temperatures (>30K).

Superconductors, both Type I and Type II, are bounded by three factors – current density, temperature and magnetic field. When Onnes first discovered superconductivity, his dreams of constructing large electromagnetic devices was quickly stalled by the realization of these limits. Therefore, in the construction of superconducting devices, it is the constant challenge of optimizing these limits that characterized the work of the magnet engineers and research scientists. To date, superconductivity has been applied to many areas, some successfully, some not quite. Below are some devices that have been or are in the process of being constructed:

1. Research magnets for high energy physics applications;
2. Controlled thermonuclear fusion reactors;
3. Magnetohydrodynamic (MHD) generators;
4. Direct Current (DC) and Alternating Current (AC) generators/motors;
5. Energy storage systems;
6. Magnetic levitation trains;
7. Magnetic separation devices;

8. Nuclear magnetic resonance (NMR) devices;
9. Magnetic resonance imaging (MRI) devices.

Throughout the years, discoveries and researches in superconductivity have also inspired many theories that have elicited much understanding on this topic. These works have led to the awarding of the Nobel Prize to various individuals. Below are selected Nobel Prizes awarded for work done in superconductivity:

Table 1.1a Nobel prizes awarded in the area of superconductivity

Year	Area	Individual	Research
1913	Physics	Heike Kammerlingh Onnes	Discovery of superconductivity in mercury
1972	Physics	John Bardeen, Leon Cooper, John Schrieffer	BCS theory for explaining superconductivity
1973	Physics	Brian Josephson, Leo Esaki, Ivar Giaever	Discovery of the Josephson effect
1986	Physics	Alex Muller, Georg Bernorz	Discovery of high-temperature superconductors
2003	Physics	Alexei Abrikosov, Vitaly Ginzburg, Anthony Leggett	GLAG theory for explaining superconductivity and superfluidity

In addition to these individuals, the area of superconductivity has also spawned much scientific progress in other areas related to the development of MRI and NMR, which led to many other discoveries.

1.2 High Temperature Superconductors (HTS)

The discovery of HTS occurred in 1986 when Muller and Bernorz of IBM Research Laboratory in Zurich synthesized a ceramic compound that had a critical temperature of 35K. The discovery broke the lull in superconductivity research and initiated a flurry of activity, particularly for the search of superconductors in a class that was never thought possible to demonstrate the effects of superconductivity. A year later, in 1987, the compound YBaCuO (YBCO) was discovered by researchers led by Paul Chu from the University of Houston with a critical temperature of 93 K. This significant jump in critical temperatures marked an important step in the commercialization of superconducting technologies because the cryogenic requirements became less demanding than those at liquid helium temperatures. With HTS, liquid nitrogen, which is inexpensive, could be used as the cryogen to maintain a suitable operating environment for superconductors.

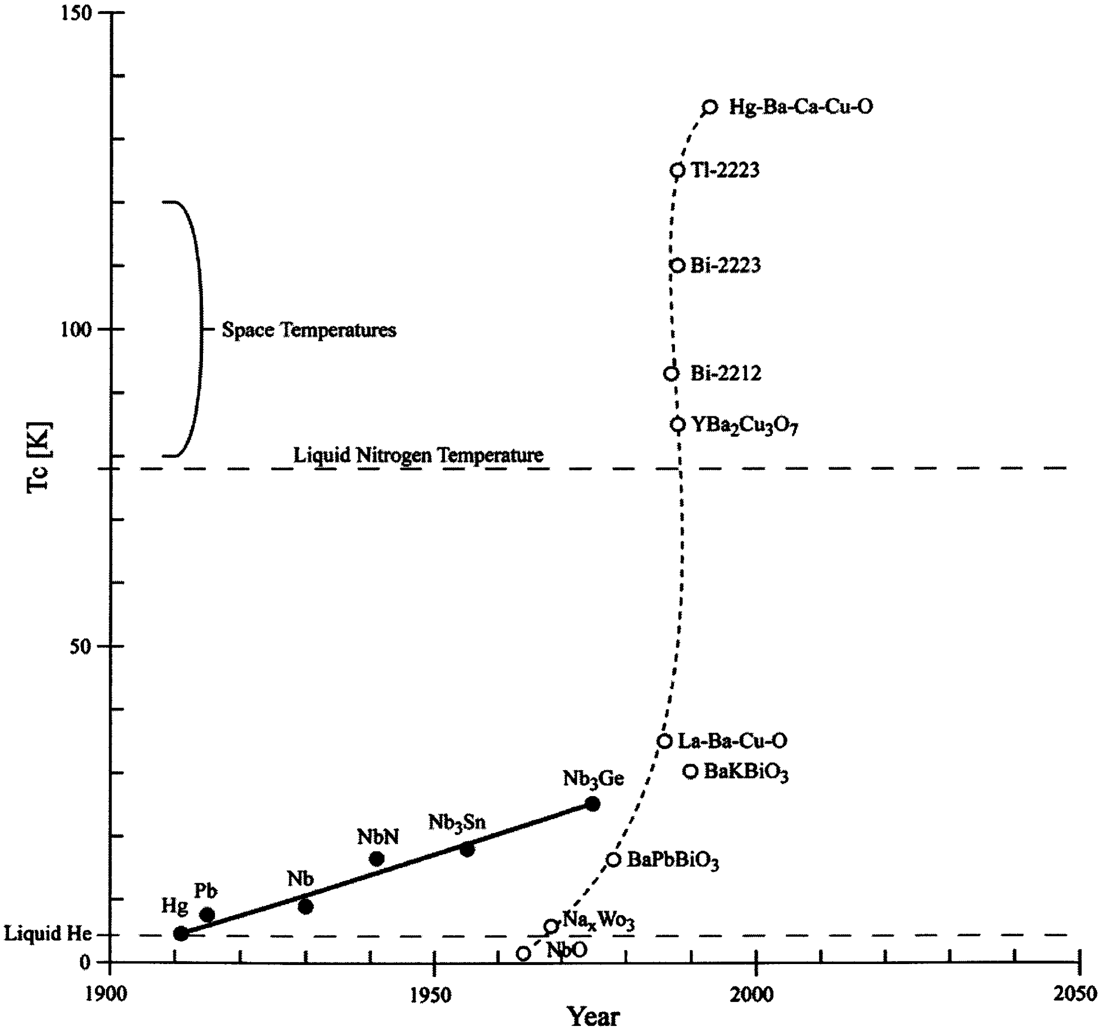

Figure 1.2a Evolution of T_c with new discoveries of superconductors over time [1]

Apart from having high critical temperatures, HTS also has the ability to sustain high current densities in large background fields. This makes HTS very promising in high-field applications. At the time of this writing, several significant advances have been made in the application of HTS. Among these applications include superconducting ship propulsion motors and generators, synchronous condensers that stabilize grid voltages and superconducting magnetic energy storage (SMES) systems. Though many of these applications are presently not yet commercially available, the promise HTS holds for the future are certainly exciting.

1.3 Issues with YBCO

Even with its cryogenic advantages, the application of YBCO in commercial applications has not been widespread due to many economic and operational concerns; the most important of which is the high manufacturing cost of the YBCO which is available in the form of tape. Complications in the manufacturing process of the tape enters as materials scientists continue to create long lengths of continuous tapes that are highly homogenous and can handle high current densities. Needless to say, high current densities are desired for efficient operation of magnets. To date, current densities of up to 17,000 A/cm^2 have been achieved by the first generation YBCO tapes manufactured by American Superconductor Corporation (AMSC).

In addition, operational issues have also limited the application of YBCO to other devices. Generally speaking, for HTS, operating both under cryostable and adiabatic conditions, the issue of stability, which is the ability of the magnet to operate steadily in the presence of disturbances, is no longer a critical issue. This, of course, is subject to the magnitude of the energy disturbance, on which there will be more elaboration in Chapter 2. Protection, which is the ability to protect the winding from permanent damage in the event of a failure mode, still remains an issue that needs further study and development.

There are three sub-issues in protection that needs to be addressed:

1) Overheating
2) High internal voltage
3) Overstressing

As in LTS, overheating is the primary threat to high-field magnets because of its rapid transition from superconducting to normal state. The stored in the magnet is converted into thermal energy and could cause a meltdown within the winding layers during a quench. Particularly for magnets in driven mode, occurrences of normal zones can quickly precipitate hot spots in the magnets, and cause thermal runaways to occur. Related to the issue of overheating is the issue of high internal voltage. As will be more clearly explained in Chapter 3, the emergence of resistive zones in magnets can cause a high voltage that is hardly detectable at the terminals of a persistent magnet or at regions far away from the heated zone. High internal voltage can cause a high voltage arc and punch a hole through the conductors. This phenomenon has been observed in actual cases. Finally, high temperature differentials that occur during quenching also induce thermal strains. In addition of being exposed to high Lorenz forces during operation, thermal strains can cause degradation to the conductors or positively feedback into the propagation of resistive zones.

1.4 Overview

In this thesis, all three of these protection sub-issues will be addressed. In Chapter 2, the issue of overheating is studied. Particularly, for the magnet designer, as was explained in the paragraph above, the sources of high internal voltage and overstressing occurs because of heating within the winding layers. Therefore, the best strategy to improve protection is to minimize events of overheating and non-recovering quench events. To this end, the idea of increasing heat propagation within winding layers, to minimize localized temperature spikes, becomes an attractive passive protection strategy. A simple but elegant approach would be to improve overall thermal conductivity of the magnet by replacing the generally less thermally conductive electrical spacers with more thermally conductive ones. Apart from that, there was also the need to observe how contact resistance varies with pressure and spacer materials as they both affect the heat propagation characteristics of the magnet.

In Chapter 3, the issue of high internal voltage is studied in a small test coil assembly. The demonstration of how high internal voltage occurs is not an issue that has previously been widely studied. Even though in the past, many failures and permanent damages have been attributed to the occurrences of high voltage, not much is known about its characteristics and profile in a quench event.

The idea of thermally induced strains is studied in Chapter 4. However, the approach taken here is not to study how failure occurs from stresses, but rather to use the presence of these stresses to indicate the occurrence of quenching. The technology in use here is acoustic emission (AE), which detects acoustic waves that are generated by strains in the magnet. More simply, the AE sensor 'listens' to the magnet to hear cracks that occurs during quenching so that efforts can be actively taken stall the quenching process. Previously, AE sensors have been used in LTS magnets to detect events such as mechanical wire motion, epoxy cracking and so forth. Our approach represents an effort to extend this technique to a less obvious role of detecting thermal induced cracking in magnets.

Finally, our findings will be summarized in Chapter 5, where suggestions for better magnet protection strategies are presented. The conductor that most of the experiments are performed on are YBCO conductors, in the form of tape; our work hopefully will sheds light of key operational issues that bring a step closer to commercialization of highly effective HTS superconductors.

Chapter 2 – Overheating

For the most part, a particular advantage of using HTS over LTS in high-field applications is its stability against quench occurrences. Because of its low index number, the transition of HTS from the superconducting to normal zone is fairly gradual in comparison to LTS, and aids in the enhancement of stability in HTS. In LTS, quenches can be induced by the slightest amount of energy input, in the order of 0.2 mJ/cm^3, which can be caused by epoxy cracking, conductor motion, and heat leaks. For HTS, the threat of overheating comes primarily from damages in the conductor, joule heating from resistive joints, and heat leaks from the cryostat. Therefore, even with its stability, a magnet designer has to prepare for the occurrences of quenches to protect the coil.

2.1 Energy Balance

The investigation of overheating in superconducting magnets begins most simply with the examination of the power density equation:

$$C_{cd}\frac{\delta T}{\delta t} = \nabla(k_{cd}\nabla T) + \rho_{cd}J_{cd}^{2} + Q_{gen} - Q_{cooling} \qquad (2.1\text{ a})$$

which describes the power density balance within a specific winding volume. In Equation 2.1 a, C_{cd} is the volumetric heat capacity of the conductor, k_{cd} its thermal conductivity, ρ_{cd} the electrical resistivity and J_{cd} its current density. Finally, the last two terms on the right hand side Q_{gen}, and $Q_{cooling}$, represent, respectively, the energy generated by a thermal disturbance and the heat removed through cooling of the cryogen. This equation is no more than a power balance equation which states that the heat generated within a winding can be stored in the form of thermal energy density and/or removed via conduction and/or convection.

For an adiabatic magnet, the term $Q_{cooling}=0$. In the event that a thermal disturbance occurs in the magnet, to maintain stability, the heat generated, Q_{gen}, which precipitates joule heating, $\rho_{cd} J_{cd}^2$, would have to be entirely absorbed by the winding pack. Therefore, in transient condition

$$C_{cd}\frac{\delta T}{\delta t}+\nabla(k_{cd}\nabla T)>\rho_{cd}J_{cd}^2+Q_{gen} \qquad (2.1\text{ b})$$

would have to be achieved to keep the magnet stable and superconducting at all times. If the reverse were true, where the heat generation is larger than the power dissipated through conduction and stored within the winding layers, the normal zone will continue spreading until a minimum propagation zone (MPZ) is achieved and a thermal runaway will subsequently occur. In driven mode, the quenching process will occur until the power supply is shut; in persistent mode, all the magnetic energy stored within the winding, $\frac{B^2}{2\mu_0}$, will be discharged through the heated zone.

In steady state condition, however, when the heat capacity around the heating area is filled and the transient extraneous energy Q_{gen} disappears, the condition below has to be fulfilled to maintain stability.

$$\nabla(k_{cd}\nabla T)>\rho_{cd}J_{cd}^2 \qquad (2.1\text{c})$$

In both steady state and transient condition, it can be seen that the overall thermal conductivity of the magnet is vital to sustain stability. When the overall thermal conductivity is large, for a given amount of heat generation, the temperature differential becomes smaller.

Conditions 2.1b and 2.1c, however, can only be maintained when a permissible level of energy, Q_{gen}, is generated; above that threshold, an MPZ is achieve and joule heating causes a full quench. Table 2.1a presents some typical values for the "energy margins", E_{mx}, allowed in an adiabatic HTS magnet and the maximum allowable temperature excursion, $[T_{op}]_{mn}$, from its operating temperature.

Table 2.1a Energy margins and allowable temperature excursions in HTS magnets [17]

Winding	T_{op}[K]	$[T_{op}]_{mn}$ [K]	E_{mx}[mJ/cm^3]
HTS	4.2	20	300
	10	15	700
	30	10	3700
	70	5	8400

2.2 Transverse and Longitudinal Dissipation

In adiabatic conditions, when a localized heating occurs in a winding pack, thermal diffusion occurs in the area around the heated zone. For a solenoid constructed by stacking multiple pancakes, heat propagation in the longitudinal and transverse direction within the heated pancake would be significantly larger than the propagation between pancakes because of higher contact resistance between pancakes.

Normal-zone propagation (NZP) velocity quantifies the speed at which the normal zone spreads out in the winding when heating occurs. It is of particular importance because during a quench, a magnet with high NZP velocity will be able to dissipate thermal disturbances over a large volume. This reduces the occurrences of temperature spikes within the winding that can cause degradation and meltdown of the conductors. Therefore, by enhancing a magnet's NZP velocity, the magnet would have better self-protection properties.

From [2], under steady state conditions where $\nabla(k_{cd}\nabla T) = \rho_{cd} J_{cd}^2$, the NZP velocities in the longitudinal direction, U_l, and in the transverse direction, U_t, are given as such:

$$U_l = \frac{J_m}{C_{cd}}\sqrt{\frac{\rho_m k_m}{(T_t - T_{op})}} \qquad (2.2\text{ a})$$

$$U_t = \frac{J_m}{C_{cd}} \sqrt{\frac{\rho_m k_i \delta_{cd}}{2\delta_i (T_t - T_{op})}} \qquad (2.2\text{ b})$$

In the equations above, k, and δ denotes thermal conductivity and thickness, while the subscripts m, cd, and i correspond to matrix, conductor and insulation respectively. The temperature $T_t = \frac{(T_{cs} + T_{op})}{2}$, where T_{cs} and T_{op} is the current sharing and operating temperature respectively.

For a YBCO tape structure given in Figure 2.2a, with matrix materials of copper, silver and nickel, U_l and U_t can be calculated. For a matrix current density, J_m, of 15e6 A/m^2 and a current sharing temperature, T_{cs}, of 84 K, some values for U_t and U_l are given Table 2.2a.

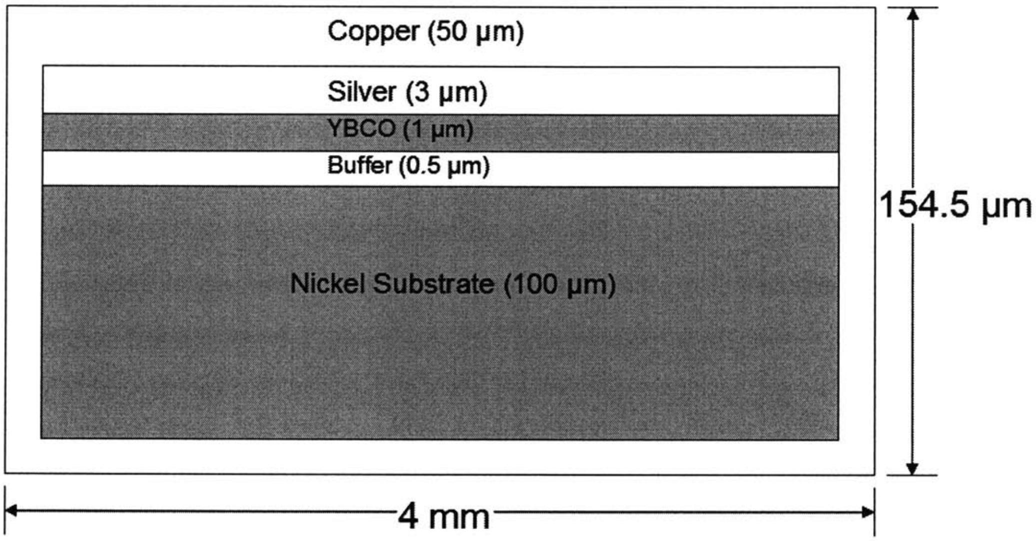

Figure 2.2a Schematic depiction of a typical YBCO composite tape cross section.

From Table 2.2a, it is observed that the longitudinal NZP for the YBCO composite tape has a calculated value of 3.69 mm/s. The transverse NZP velocity however varies significantly with the spacer material; and more precisely, with the thermal conductivity of the spacer. From Table 2.2a, it is observed that for 76 µm thick diamond spacers, U_t

could be improved significantly (>250 U_t of Nomex) because of its high thermal conductivity (~10,000 W/m-K). At present, only Nomex is used as a spacer in magnets; copper (II) oxide and diamond, however, appear promising as they both can significantly increase U_t and enhance protection in magnets. These issues will be explored more deeply in the following sections.

Table 2.2a Longitudinal and transverse NZP velocity for various spacer materials for YBCO composite tape

Thickness [μm]	Spacer Material	U_t [mm/s] *(Calculated)*	U_l [mm/s] *(Calculated)*
25.4	Nomex®	0.15	3.69
76		0.09	
76	Copper (II)	9.35	
76	oxide	5.40	
254	Diamond	24.20	
		13.26	

2.3 Thermal Diffusivity and Transient Diffusion Time

It should be clear by now that the ability to diffuse disturbance energy as quickly as possible within an adiabatic coil enhances protection in a magnet because it reduces the temperature spike, which can lead to degradation or permanent damage of the superconductor. Therefore, the selection of layer-to-layer spacer materials that promotes heat diffusion could be a good passive protection technique.

In an adiabatic coil, assuming that a temperature distribution arises within a given winding volume due to a extraneous heat input e.g. a heat leak or hysteresis, and that joule heating, and internal generation are negligible, Equation 2.1a reduces to:

$$C_{cd}\frac{\delta T}{\delta t} = \nabla(k_{cd}\nabla T) \tag{2.3a}$$

$$\frac{\delta T}{\delta t} = \frac{k_{cd}}{C_{cd}}(\nabla^2 T)$$

Assuming a one-dimensional conduction, in the x-direction, and constant temperature boundary conditions, which is usually the temperature of the operating cryogen, the temperature of the magnet as a function of space and time are given by [3] as:

$$T(x,t) = \frac{a_0}{2} + \sum_{n=1}^{\infty} a_n e^{-(\frac{n^2\pi^2 D_{th}}{\delta^2})t} \cos(\frac{n\pi x}{\delta})$$

where a's are Fourier constants, and D_{th} is known as the thermal diffusivity of the material. D_{th} is given as

$$D_{th} = \frac{k_{cd}}{C_{cd}} \tag{2.3b}$$

Using the dominant first term in the series, where $n = 1$, to approximate the transient diffusion time, τ_{tr}, we obtain:

$$\tau_{tr} = \frac{1}{D_{th}}\left(\frac{\delta}{\pi}\right)^2 \tag{2.3c}$$

A spacer material with a low transient diffusion time implies that the material can dissipate thermal energy relatively easily within its body. From Equation 2.2c, it is observed that τ_{tr} can be reduced when the material has a high value of D_{th} or a low value of thickness, δ. Due to the simplicity of these two equations, they come especially in handy for a back of the envelope calculation in selecting suitable spacer materials that can enhance self-protection in a magnet.

2.4 Insulation and Thermal Contact Resistance

Inherent in the discussions above is the assumption of zero thermal contact resistance within winding layers. This implies that a material that has a high thermal diffusion rate might in principle appear to be a good spacer, but in reality might not - if its thermal contact resistance with other materials is high, and retards heat propagation.

Contact resistance arises primarily from microscopic gaps that exist between two surfaces in contact. Naturally, the rougher the surface of a material, the higher is its thermal contact resistance. Because of these gaps, heat transfer between the two surfaces through conduction is greatly reduced. Thermal contact resistance, however, can be reduced in the presence of interfacial fluids with good thermal conductivity or increased contact pressure that minimizes the gaps. Table 2.4 a illustrates typical values of contact resistances between aluminum interfaces at different pressures and interfacial fluids.

Table 2.4a The effects of pressure on contact resistances under vacuum conditions [4]

Contact resistance *(Contact pressure)*	$[10^{-4} \frac{m^2K}{W}]$ *(100 kN/m^2)*	$[10^{-4} \frac{m^2K}{W}]$ *(10,000 kN/m^2)*
Aluminum	1.5-5.0	0.2-0.4
Copper	1-10	0.1-0.5
Stainless Steel	6-25	0.7-4.0

Table 2.4b The effects of interfacial fluids on contact resistances [4]

Interfacial Fluid	Contact resistance [$10^{-4}\ \frac{m^2K}{W}$]
Air	2.75
Helium	1.05
Silicone oil	0.525
Glycerine	0.265

As can be seen, contact resistance decreases with increased contact pressure and in the presence of interfacial fluids. When compared to the thermal conductive resistance of a 25 μm thick copper shimstock (given by $\frac{\delta}{k}$ for one dimensional steady state heat transfer) of ~$6.25\text{x}10^{-8}\ \frac{m^2K}{W}$, thermal contact resistance values can be quite substantial. The thermal diffusivity, D_{th}, through winding layers would also then have to be adjusted to correctly predict the transient diffusion time, τ_{tr}, of the material. This can be done by finding an effective thermal conductivity, k_{eff}, in the material.

In the following sections of this chapter, two sets of experiments are presented to test two main issues discussed in the sections above, namely, the effects of

1) insulation spacers on heat diffusion, and,
2) thermal contact resistance on the transverse heat transfer.

2.5 Experiment I –The Effects of Copper Oxide and Nomex® Spacers on Layer-to-Layer Heat Propagation during the Quench of a Single YBCO Pancake Coil

2.5.1 Experiment Overview

In this experiment, a single pancake coil of five layers was wound using a YBCO tape; see Figure 2.5.1a and Table 2.5.1a for details. The coil was separated into two halves – one containing spacer materials made of Nomex, a synthetic aromatic polyamide polymer produced by DuPont and the other containing copper (II) oxide spacers. Stainless steel heaters are embedded within each half of the coil, and are simultaneously activated during the experiment, to initiate a quench the coil. The voltage rise across each layer of the coil on both halves are measured and recorded through voltage taps located at every half turn of the coil. Since the heat propagation from the heaters depends highly on the spacer's thermal properties, as demonstrated in Section 2.2, the half containing the spacer with better heat propagation properties would cause a larger and faster increase in the voltage in the adjacent layers. The results can then demonstrate which spacers would be better for protection against overheating in HTS coils.

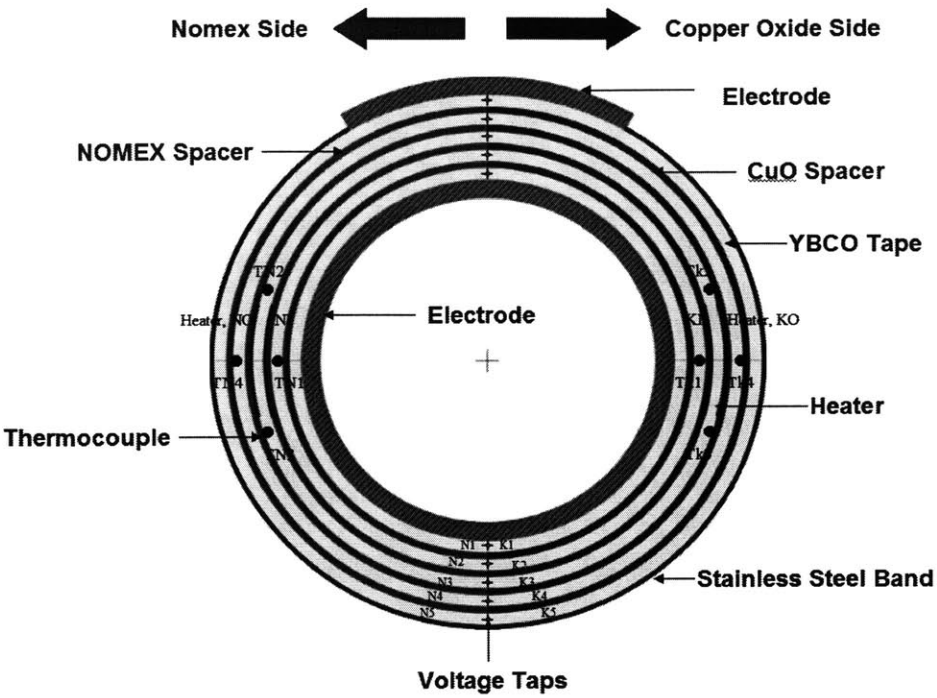

Figure 2.5.1a Schematic top view of the five-layer YBCO coil, indicating the locations of the voltage taps, thermocouples and heaters

Table 2.5.1a Details of the YBCO coil used in 2.5 Experiment I

Parameter	Value
Winding i.d. [mm]	74.9
Winding o.d. [mm]	84.0
Winding height [mm]	4.24
Number of turns	5
Operating temperature [K]	77
Effective YBCO length [cm]	~140
V_c [μv @ 1 μv/cm)	~140
I_c [A]	41

2.5.2 Apparatus and Procedure

Figure 2.5.2a shows the setup for the experiment while Figure 2.5.2b shows a close-up photograph of the actual coil and phenolic platform on which it is mounted. A Labview DAQ Instrumentation system was used to record data from the voltage taps and thermocouples.

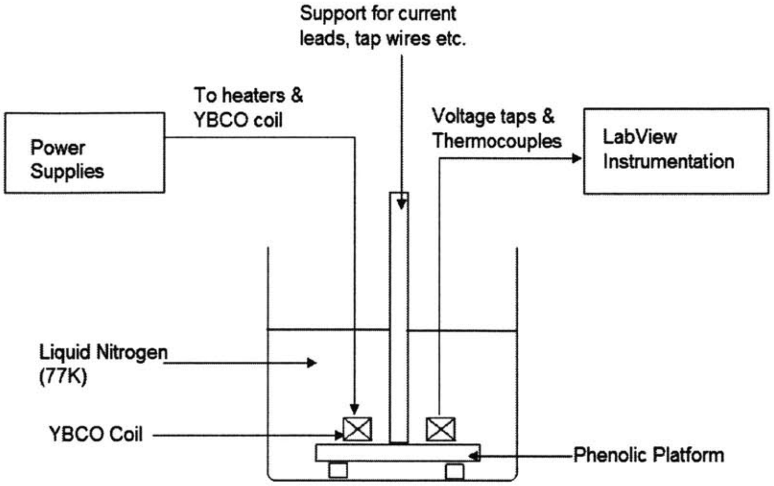

Figure 2.5.2a Schematic of the setup used in 2.5 Experiment I

Figure 2.5.2b Phenolic platform used to hold test coil

2.5.2(i) Voltage Taps, Temperature Sensors and Heaters

As indicated in Figure 2.5.1a, the five-layer coil contains ten voltage taps, with each voltage tap positioned 180° apart. The azimuthal distance between each tap is approximately 125 mm, and each tap is fabricated from a 25.4-μm thick copper shim stock. Each tap is soldered onto the surface of the YBCO tape with indium solder.

The temperature sensors are type E, Ni-Cr/Constantan thermocouples. Thermocouple Tk1 is located on the inner surface of the tape in the second layer; Tk2 and Tk3 on the outer surface of the third layer; and Tk4 on the outer surface on the fourth layer. The thermocouples on the Nomex side are also located in similar relative locations.

Four heaters are attached onto the inner and outer surfaces of the tape located on the third layer in each half of the coil. The heaters are 30mm by 4.2 mm by 25.4 μm thick, type 302 stainless steel shim stock with measured resistances of ~ 195 mΩ at 77 K. The heaters are electrically insulated with 13-μm thick Mylar tape.

2.5.2(ii) Copper (II) Oxide (CuO) and Nomex Spacers

The copper (II) oxide spacers were made "in-house" using 76-μm thick and 4-mm wide copper shimstock by heating them to 93-105 °C in a solution of sodium hydroxide (NaOH) and sodium chlorite ($NaClO_2$) for 15-20 minutes. This is a redox process that emits chlorine gas. Therefore it is vital to conduct this reaction in a hood.

The Nomex spacers used are 4 mm in width and 38-μm thick. Between each layer of the coil, two layers of Nomex spacers are used to match the spacer thickness on the copper oxide side, creating a total spacer thickness of 76-μm.

2.5.3 Results

Figures 2.5.3a and 2.3.5b show the voltage traces when heaters NO and KO are both activated simultaneously with a transport current of 17.1 A at 77 K. A step current of magnitude 9.1 A was induced in each of the heaters, creating a heating flux of ~13 W/cm^2. The heating induces a localized normal zone within the coil and the voltages are recorded by the taps.

Figures 2.5.3a and Figure 2.5.3b display results that are expected, namely, winding layers closest to the heater achieve the current sharing temperature the quickest, and that the eventual steady state voltage across each layer is a positive function of the radial distance from the heaters. However, it can be observed that the heater across the copper oxide side drives four winding layers normal, while the heater across the Nomex side only drives two layers normal. This indicates that the overall thermal diffusivity of the winding on the copper oxide side is higher than that on the Nomex side.

The maximum joule heating from the windings occurs at K4, with a magnitude of ~120 mW over an area greater than 1.5 cm^2. Given that the entire setup is submerged in liquid nitrogen, with a maximum cooling flux of ~10W/cm^2 in the nucleate boiling regime, joule heating is negligible. The heat that drives each layer normal is attributed to the heat generated from the heater.

From the results, the transverse NZP velocity can be calculated by dividing the layer thickness between each turn with the time delay it takes for the voltage across each turn to arise. Table 2.5.3a summarizes the experimental transverse NZP velocity across both halves of the coil.

Table 2.5.3a Transverse NZP velocity between layers in both copper oxide and Nomex side

Layers	Material between layers	Transverse NZP velocity, U_t [mm/s]	
		CuO side	Nomex®
4-5	76-μm spacer	0.0114	0
Heater-4	76-μm spacer	0.1360	0.042
3-Heater	25-μm Kapton	0.0318	1.500
2-3	76-μm spacer	0.0089	0

Table 2.5.3a indicates that the propagation velocity from the heater to Layer 3 is faster in the Nomex side than in the CuO side. This is because the higher thermal resistance in the Nomex® forces heat flux to flow through the Kapton® tape. The thermal resistance is given as

$$R_{th} = \frac{\delta}{k}$$

where δ is the material thickness and k is the thermal conductivity. With a little calculation, it is found that R_{th_kapton}=7.1E-5 K/W, and, R_{th_Nomex}=7.5E-4 K/W. The thermal resistance in Nomex is ~10 times less than that in Kapton tape; hence the heat flux flowing into layer three will be greater into layer four.

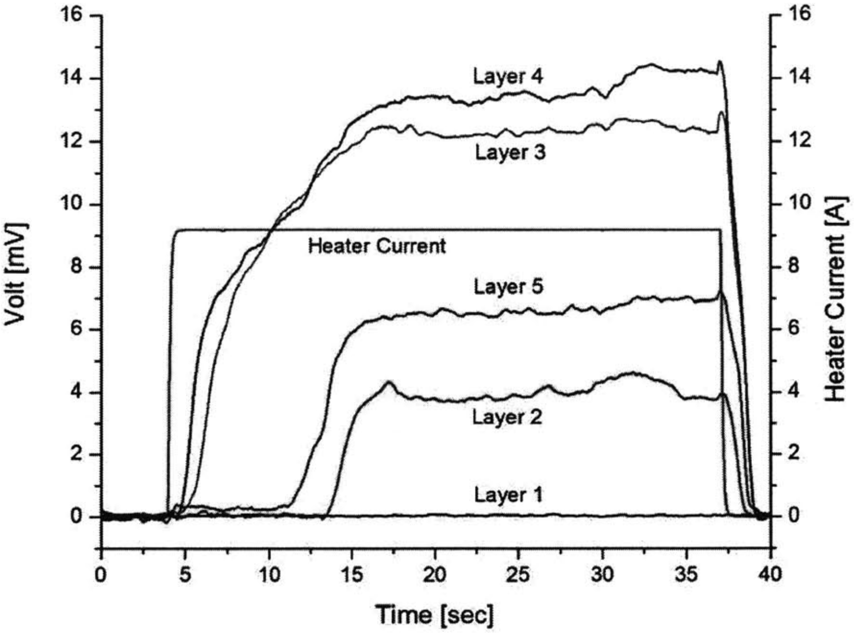

Figure 2.5.3a Voltage traces on the copper oxide side when heater KO is activated

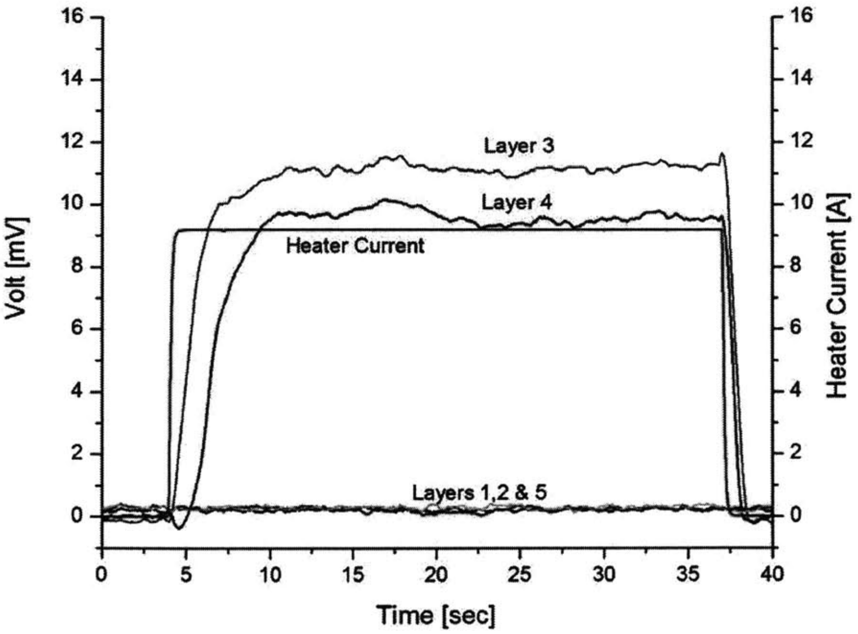

Figure 2.5.3b Voltage traces on the Nomex side when heater NO is activated

2.5.4 Conclusion

Comparing the experimental U_t with the calculated values given in Table 2.2a, we find that U_t in the CuO side is less than calculated. This implies that thermal contact resistance plays a significant role in the heat transfer between layers. Nevertheless, the experimental results clearly show that heat propagates more easily through the CuO side than in the Nomex side.

These results indicate that spacer materials with good thermal conductivity properties enhance heat propagation through the winding layers and thereby may help reduce overheating, a key to good passive protection technique. However, results also indicate that propagation through CuO is less promising than expected because of the presence of contact resistances – a topic which would be studied further in the next section.

2.6 Experiment II – The effect of thermal contact resistances and spacer materials on transverse heat propagation

2.6.1 Experiment Overview

As was demonstrated in Section 2.2 and 2.5 Experiment I, the ability of a coil to disperse localized heating in the transverse direction is greatly affected by the thermal properties of the spacer material between tape layers. In Experiment I, it has been observed that copper oxide spacers diffuse heat better than Nomex spacers because of their greater thermal diffusivity. However, not all materials with high thermal diffusivity translate into better spacer materials. An important factor that has been ignored in our analysis is the effect of thermal contact resistance. In saying that, a spacer material with good thermal properties might not be conducive for diffusing heat because the high thermal contact resistances between materials might retard the heat transfer between layers.

In this experiment, the issue of thermal contact resistance is explored by varying the compressive pressure between layers for a stack of YBCO composite tapes, and quenching the tapes through the use of stainless steel heaters much like in 2.5 Experiment I. Since thermal contact resistances exist principally through microscopic interface gaps between materials, increasing the compressive pressure between materials reduces these gaps and thus improves thermal contact. The use of interfacial fluids, such as Apiezon® grease was also employed study its reduction of contact resistance.

These series of tests extends work in Section 2.5 on the selection of good insulating materials to enhance thermal diffusion. From Table 2.2a, it is observed that transverse heat transfer can be greatly enhanced by using diamond spacers, which have thermal conductivity of ~10,000W/m-K at 100K. Therefore, in this experiment, diamond spacers, provided by Diamonex Inc. and TaiYang Inc. are used along with copper oxide spacers to test the contact resistance between superconducting layers.

2.6.2 Apparatus and Procedure

Figure 2.4.2a and Figure 2.6.2b shows the apparatus and setup used for this experiment. In this test, two layers of YBCO tape were sandwiched between two aluminum plates that provide compressive stress through the means of a pair of nuts and bolts at each end. A G10 strip is placed at the center and each side contains a heater, a spacer, and a strip of YBCO tape. Both heaters are series connected and are activated simultaneously during the experiment. The heat generated from the heaters will diffuse through the spacers and quench the superconductor. The quench voltage is then recorded via voltage taps across the tape. The spacer that propagates heat faster will cause the voltage across that half of the tape to rise first. By comparing the transient diffusion time of the spacer material and the time delay at which the quench voltage rises relative to the time at which it is heated, the effects of thermal contact resistance can be estimated. Also, by varying the compressive stress on the sample, the changes in the time taken for the voltage to rise indicates the extent to which compressive pressure can influence contact resistance.

Assuming adiabatic conditions, one-dimensional heat conduction and steady state conditions, we may model one half of the setup with a thermal constant shown in Figure

2.6.2c. As the compressive pressure between layers increase, the contact resistance is expected to decrease, hence enhancing the heat diffusion rate across layers.

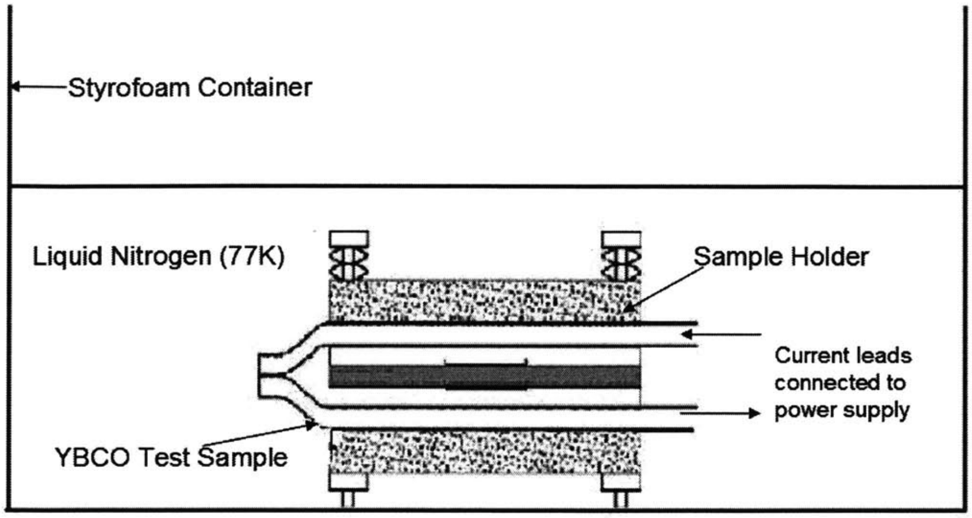

Figure 2.6.2a Experimental apparatus used in 2.6 Experiment II. See Figure 2.6.2b for greater detail on the sample holder

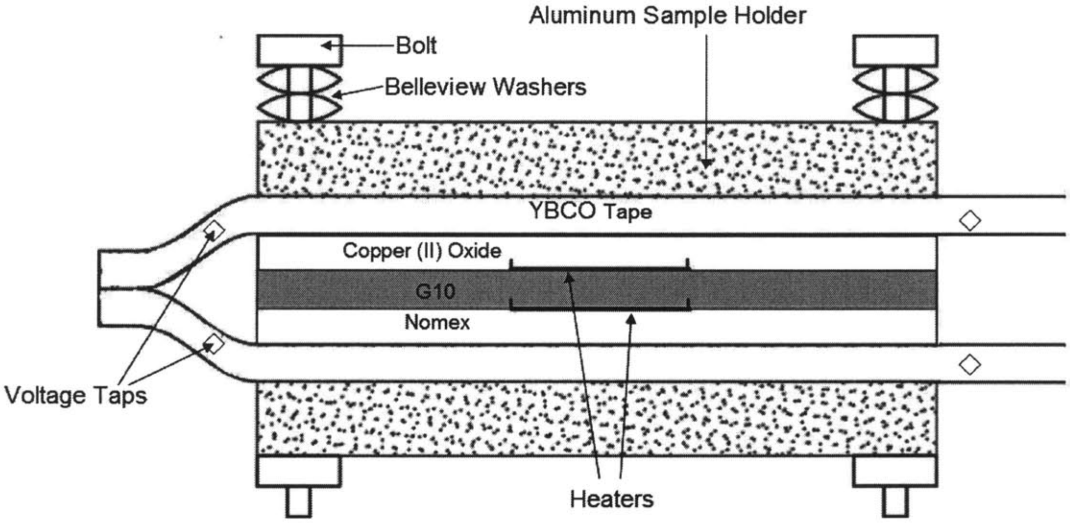

Figure 2.6.2b Side view schematic of the sample holder. The diagram is not to scale

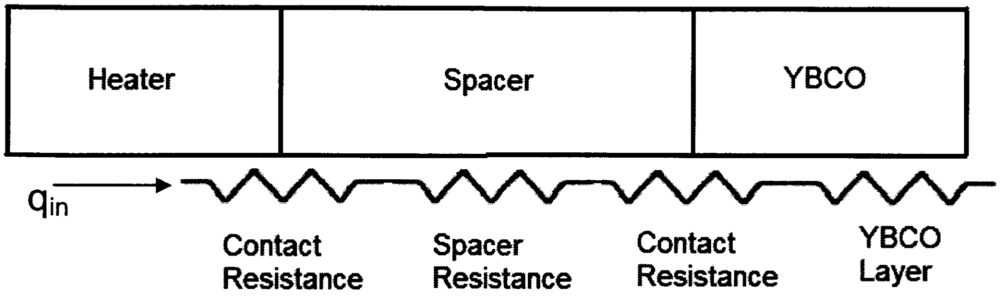

Figure 2.6.2c Thermal circuit illustration showing contact resistance at each side of the spacer between two adjacent YBCO layers in steady-state conditions

2.6.2(i) Heaters and Spacers

The heaters made are of 25.4-μm thick stainless steel shim stock; and measure 30 mm in length and 4 mm in width. The measured resistance of each heater is ~200 mΩ at 77K. The spacers are made of copper (II) oxide and diamond. The table below gives the properties of each material at 100K.

Table 2.6.2(i)a Properties of copper (II) oxide and diamond at 100K. k represents thermal conductivity, C_p, heat capacity, and ρ, density.

	k [W/m-K]	C_p [J/kg-K]	ρ [kg/m^3]
Diamond	10,000	21	3,500
CuO	482	252	8,933

With the given properties of these materials, the thermal diffusivity, D_{th}, and the transient diffusion time, τ_d, can be calculated. The results for diamond and CuO strips with varying thickness are presented in Table 2.6.2(i)b.

Table 2.6.2(i)b Calculated thermal diffusitivity, D_{th}, and transient diffusion time, τ_{tr}, for Diamond and CuO with various thickness.

	Thickness [1/1000"]	*Thickness* [μm]	D_{th} [m^2/s]	τ_{tr} [s]
Diamond	10	254	0.136	4.8E-8
CuO	1	25.4	2.14E-4	3.05E-7
CuO	3	76	2.14E-4	2.75E-6

It can be observed from the table above that a 254-μm thick diamond spacer has a transient diffusion time ~6.4 times less than that of a copper oxide strip ten times thinner. Therefore, in the absence of thermal contact resistance, the voltage across the diamond side should rise before the copper oxide side during heating.

2.6.2 (ii) Belleville Washers

The Belleville washers used in this test were size #8, nickel alloy washers. The washers were stacked in series and the bolts were tightened using a torque wrench. By converting the amount of torque applied to each bolt, the compressive pressure on the sample can be calculated.

2.6.3 Results

The compressive loads on the tape were varied from 0 MPa to 32 MPa. The samples were heated and the voltage rises from taps were recorded. Figure 2.6.3a shows the output of a trial run and how the time delay between the activation of the heater and voltage rise in Diamond is recorded. For each compressive load, the tests were repeated ten times and the average and standard deviation of the time delays are plotted on error-bar graphs.

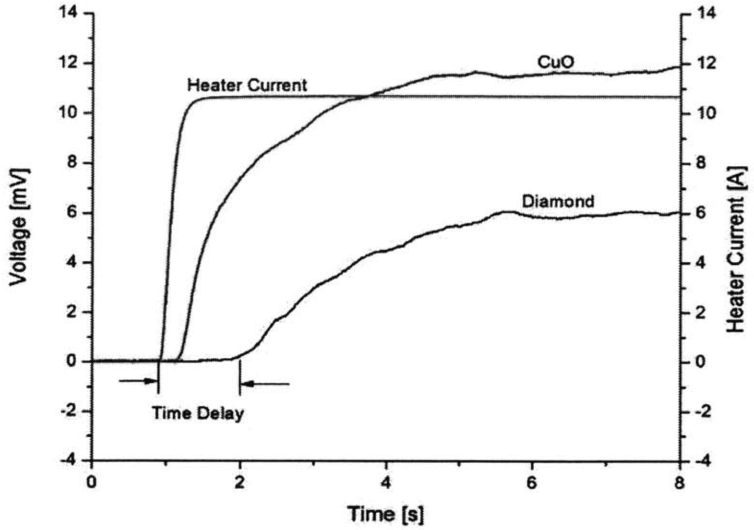

Figure 2.6.3a Illustration of how the time delay between the activation of the heater and the voltage rise in the YBCO tape across the half containing diamond is calculated

In the first test, a 254-μm thick diamond spacer and a 76-μm thick copper oxide spacer were tested. The transport current through the tape was 30 A or ~0.71 of I_c and the heat flux input in the heater was ~19 W/cm^2. From the results of the time delays are given in Figure 2.6.3b, it is evident that as compressive pressure on the samples increase, the magnitude of the time delays decreases because the interfacial gaps between the spacer and superconductor decreased with increasing pressure. However, at all pressures, it can be observed that copper oxide is a better spacer as the time delay is smaller than that in the diamond spacer in every trial test. This result is surprising as the thermal diffusion times for diamond and copper oxide are, respectively, ~0.05 μs and ~3 μs. This implies that heat should propagate approximately 60 times faster in diamond than in copper oxide and the time delays given in Figure 2.6.3b should indicate that the time delays for the voltage rises should be longer in the copper oxide half of the sample. The fact that this is not true is attributed to the effect of contact resistance between spacers.

In the second test, a copper oxide spacer was tested against a diamond spacer with Apiezon grease. From the results of the test given in Figure 2.6.3c, it is observed that the

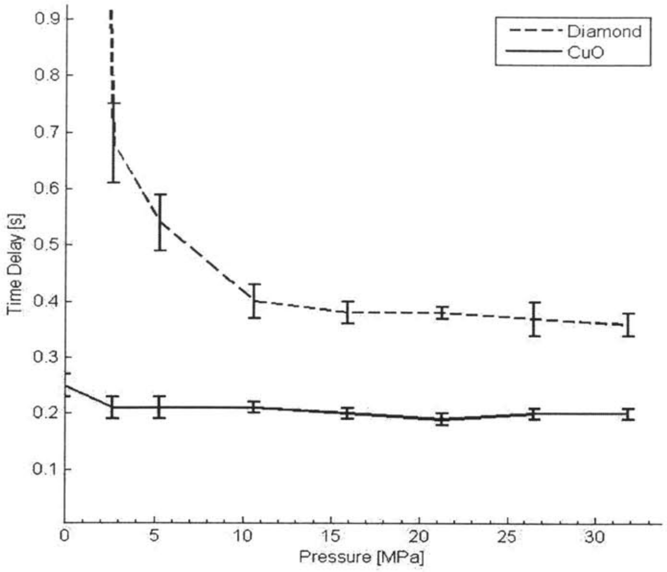

Figure 2.6.3b Difference in time delay for diamond and CuO spacers

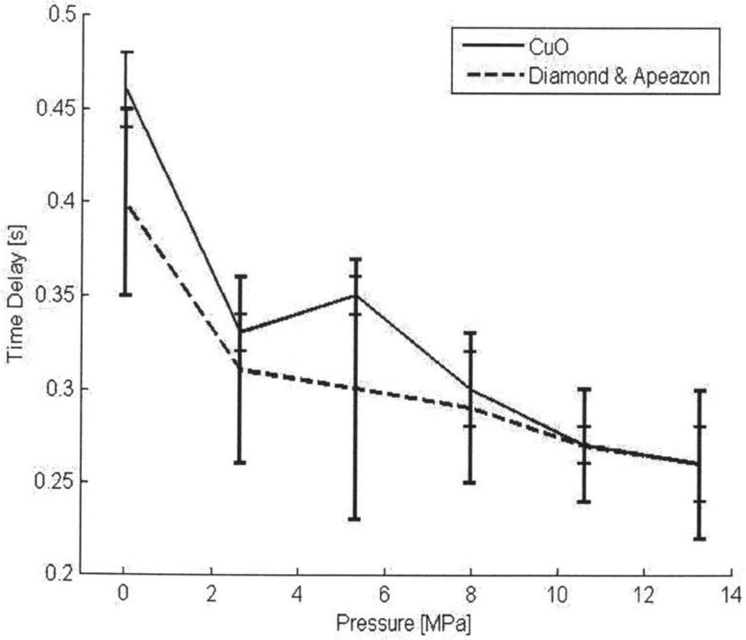

Figure 2.6.3c Difference in time delays between copper oxide and diamond spacer with Apiezon grease

mean differences in delay time for both spacers have been greatly reduced, and that the Diamond spacer actually diffuses heat faster than CuO for pressures below 11 MPa. Thus it can be seen that Apiezon grease does significantly reduce thermal contact resistance and enhance the ability of a spacer to diffuse thermal energy.

2.7 Chapter Summary

In this chapter, the role of spacer materials and thermal contact resistance in enhancing protection measures against overheating in HTS coils has been explored. It has been observed that spacers with good thermal diffusivity characteristics do improve transverse NZP, and reduce localization of hot spots in the coil. 2.5 Experiment I clearly demonstrated that a copper oxide spacers propagate heat through the layers better than Nomex spacers do. From this observation, a natural thought progression would be to use materials with extremely high thermal diffusivities as spacers. In 2.6 Experiment II, diamond spacers were used and compared with copper oxide spacers to explore its efficacy in protection against overheating. Experiment II results however showed that diamond was not as effective as copper oxide in diffusive heat energy. The reason for this is because of its high thermal contact resistance. Using Apiezon grease, it was shown that thermal contact resistance could be reduced. Therefore, it is concluded that, apart from a high thermal diffusivity rate, a spacer material needs to have low thermal contact resistance with the adjacent tape layers to provide good heat transfer in the event of a quench.

Chapter 3 - Internal Voltage

For a magnet operating in persistent mode, where the terminals are shorted by a superconducting persistent switch, the initiation of a normal zone within the winding layers generate a voltage only within the coils that is not detectable via voltage taps at the terminals. This internal voltage is determined by the resistance within the winding and the inductance of the coil.

This phenomenon of internal voltage is an issue which, to date, has not been very well studied, but has been attributed to the damage and destruction of some large-scale LTS magnets in the past. In this chapter, the occurrence and characteristics of the internal voltage phenomenon, in HTS magnets, is studied in order to enhance techniques to protect HTS magnets. Experiments are conducted on small test coil assemblies, and the results are compared to those of a numerical model.

3.1 Concept Introduction

As mentioned, internal voltage occurs when a normal zone is generated within a coil, creating a resistive voltage. The magnitude of this voltage depends highly on the normal zone volume and the rate at which this normal zone appears because the current for a coil in persistent mode decays with time. Figure 3.1a shows the voltage distribution for a magnet with both ends grounded and with various fractions of the magnet in normal state at an instant in time. It should be noted that the maximum internal voltage, V_{int}, is given by Iwasa [14], as

$$V_{\text{int}}(t) = f(1-f)R_{NZ}I(t) \qquad (3.1a)$$

where f is the fraction of the coil that is normal, R_{NZ} is the resistance of the normal zone and $I(t)$ the time dependant transport current through the coil.

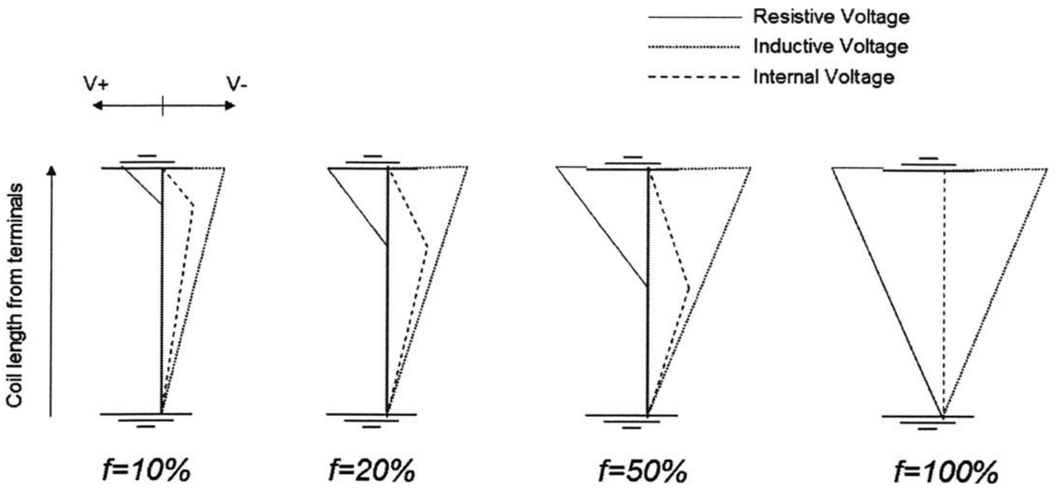

Figure 3.1a Voltage distributions across a magnet with its terminals shorted with various resistive volumes. The coil conductor is stretched from one terminal to another, and the resistive voltage represents where quenching occurs. The inductive voltage compensates for the quench and a resulting internal voltage, which is the summation of both the resistive and inductive voltages, is obtained. (Adapted from Iwasa[14])

From Equation 3.1a, it can be observed that the internal voltage is a parabolic function of *f,* and the maximum internal voltage can be easily found by taking the derivative of V_{int} and setting it equal to zero.

$$\frac{dV_{\text{int}}}{df} = (1-2f)I(t)R_{NZ} = 0$$

Solving the equation above, $f = \frac{1}{2}$.

As demonstrated in Figure 3.1a, the maximum internal voltage occurs when 50% of the coil goes normal. On the other hand, when the entire coil is normal, f = 100%, no internal voltage occurs. It should be noted that the phenomenon above is present only when the current through the coils are equal in all four cases and the terminals are grounded.

3.2 Example of the internal voltage in a two coil magnet system

Consider a magnet comprised of two coils, Coil 1 and 2, in persistent mode as shown in Figure 3.2a. A current is induced in the loop when the persistent switch, *PS*, is turned off, and current, *I*, flows through two coils, with inductances, *L1* and *L2*. Consider also the presence of a resistance, *R*, in the loop, which arises from a quench in Coil 2.

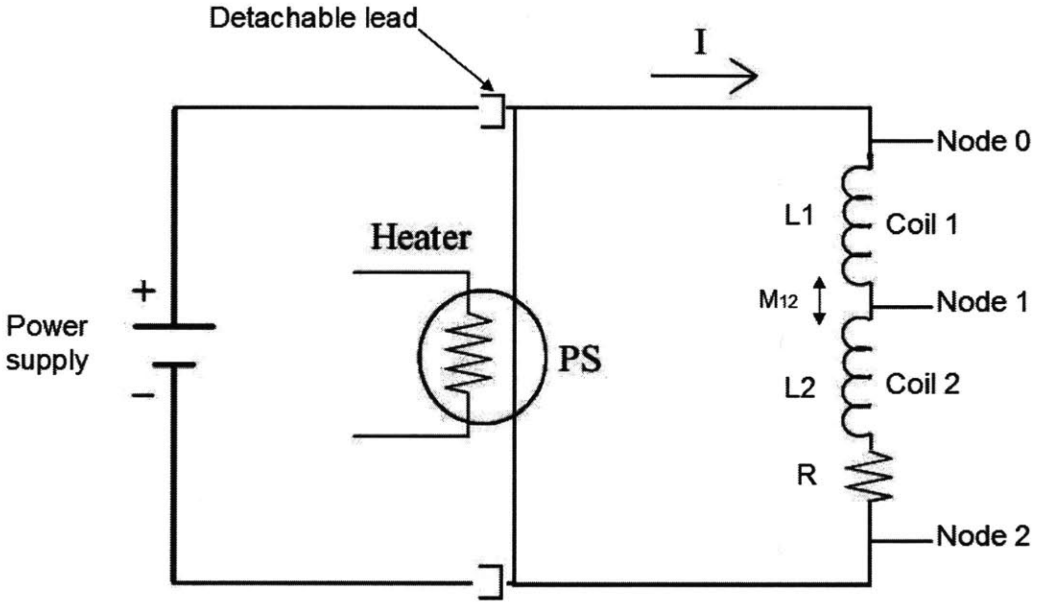

Figure 3.2a Simple configuration of a magnet in persistent mode

The presence of a resistance in the loop generates a voltage within Coil 2. Let V_{10} be the voltage across Nodes 1 and 0 (Coil 1), and V_{21} be the voltage across Nodes 2 and 1 (Coil 2), we have:

$$V_{10} = -(L_1 + M_{12})\frac{dI}{dt} \tag{3.2a}$$

$$V_{21} = -(L_2 + M_{21})\frac{dI}{dt} - IR \tag{3.2b}$$

where M_{12} is the mutual inductance between Coils 1 and 2, and $M_{12} = M_{21}$. Summing the voltage about the loop, we know that $V_{20} = 0$. Therefore,

$$V_{10} + V_{21} = 0 \Rightarrow V_{21} = -V_{10}$$

$$\therefore IR = -(L_1 + L_2 + 2M_{12})\frac{dI}{dt}$$

Let $(L_1 + L_2 + 2M_{12}) = L_{Tot}$ and assuming that R is constant, the simple first-order differential equation can be integrated as such

$$\int\frac{dI}{I} = \int -\frac{R}{L_{Tot}}dt$$

Using the initial condition that $I(t=0) = I_0$, the expression for the current in the loop is thus

$$I(t) = I_0 e^{-\frac{t}{\tau}} \tag{3.2c}$$

where $\tau = \frac{L_{Tot}}{R}$, which is the time constant, at which the current decays to 63% of its initial value. As can be seen from Equation 3.2a, the presence of a resistance causes dissipation and decay of the current in the loop.

Assuming that the rise in resistance in the coil is a linear function of time, $R(t)=at$, where a is a constant and when the temperature of the superconductor is greater than the current sharing temperature,

$$I(t) = I_o e^{-\frac{at^2}{2L_{tot}}}$$

$$V_{21} = -\left(1 - \frac{(L_2 + M_{12})}{L_{Tot}}\right) I(t)R(t)$$

$$V_{21} = -\left(1 - \frac{(L_2 + M_{12})}{L_{Tot}}\right) I_o a e^{-\frac{at^2}{2L_{tot}}} t \qquad (3.2d)$$

As we can see from Equation 3.2d, if L_{Tot} gets large, and all the other parameters remain the same, the rate of current decay decreases, and the voltage V_{12} can potentially can very large. Figure 3.2b shows a qualitative representation of how each variable will vary when *R(t)=at.*

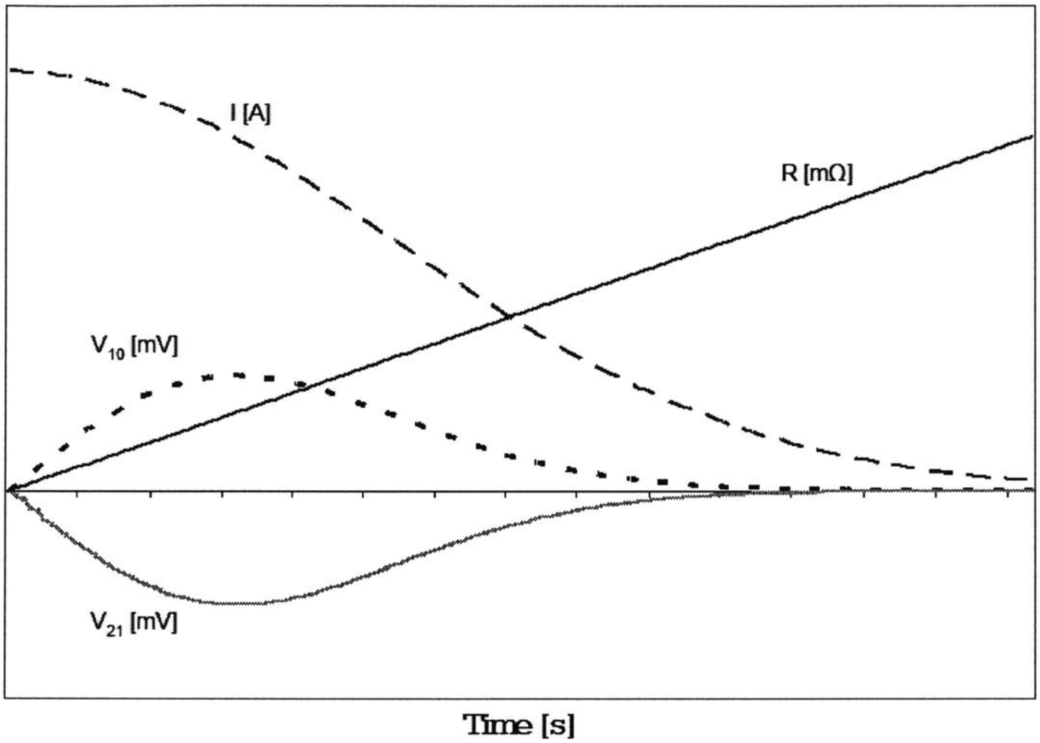

Figure 3.2b Illustration of how current, resistance and voltages in the loop vary with time during quenching in persistent mode

As can be observed from Figure 3.2b, as *R(t)* rises, the current in the loop, *I(t)*, decays rapidly and the voltages in the loop, V_{10} and V_{21}, reaches a maximum and eventually goes to zero as *I(t)* fully decays. Looking at the voltage across the coil where V_{10} is not zero, the voltage profile shown in Figure 3.2c is expected to have arisen in the coils. It should be noted that the inductive voltage profile is not linear as depicted in the figure.

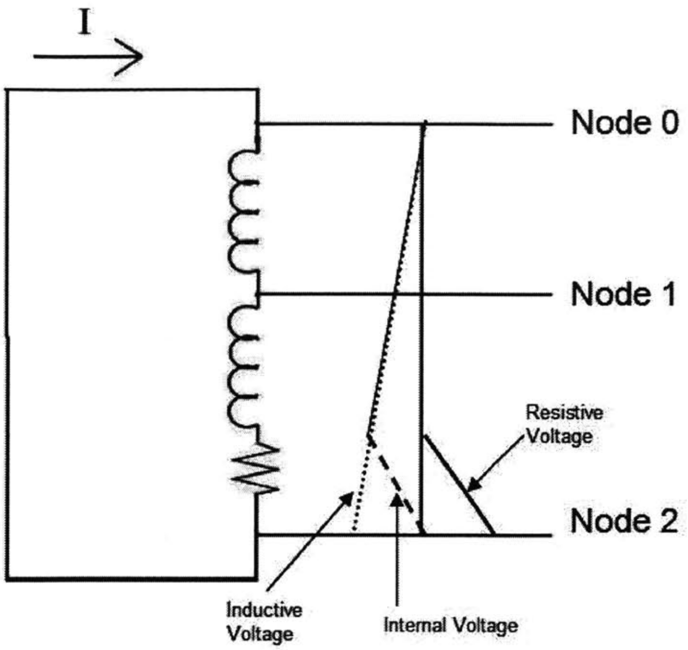

Figure 3.2c Internal voltage profile across coil at any instance of time during quenching and before *I(t)* fully decays. The magnitude of the voltages varies with time.

3.3 Experiment I – Internal voltage in two single pancake YBCO coils

3.3.1 Experimental Overview

In this experiment, two single pancake YBCO coils are used to demonstrate the effect of internal voltage during a quenching process. The two pancakes are connected in the configuration of the electrical circuit shown in Figure 3.2a, where the coils can be charged up and put in persistent mode. During that time, a heater is activated to quench one or both coils. Voltage taps located within the coil windings are used to record the voltage generated from within the coils.

3.3.2 Apparatus and Procedure

Figure 3.3.2a presents the setup used in this experiment. Two YBCO coils with inductances of 690 μH each, were connected to form a close loop. A stainless steel heater in the shape of a doughnut was adhered using epoxy to one surface of a coil and was used to drive the coil normal to simulate a quench. The entire system is submerged in liquid nitrogen (77 K) and the quenching process is conducted in persistent mode. Figure 3.3.2b presents the electrical circuit of the test setup while Figure 3.3.2c shows a photograph image of the setup.

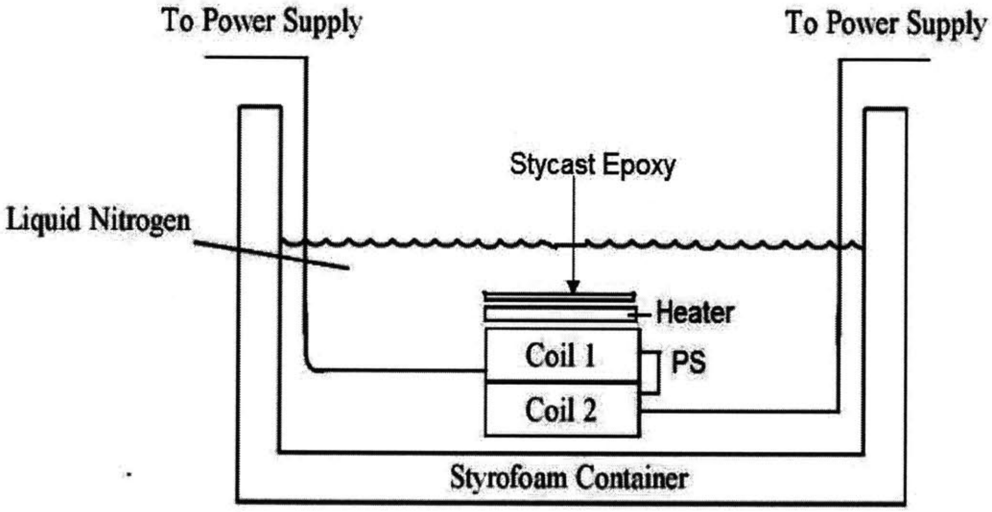

Figure 3.3.2a Experimental setup for internal voltage test

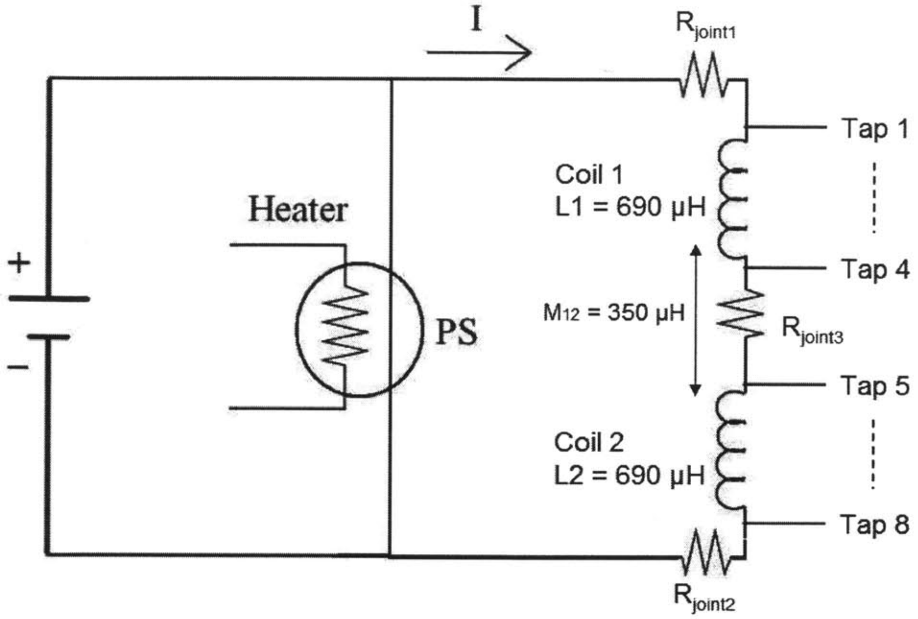

Figure 3.3.2b Electrical circuit diagram of setup

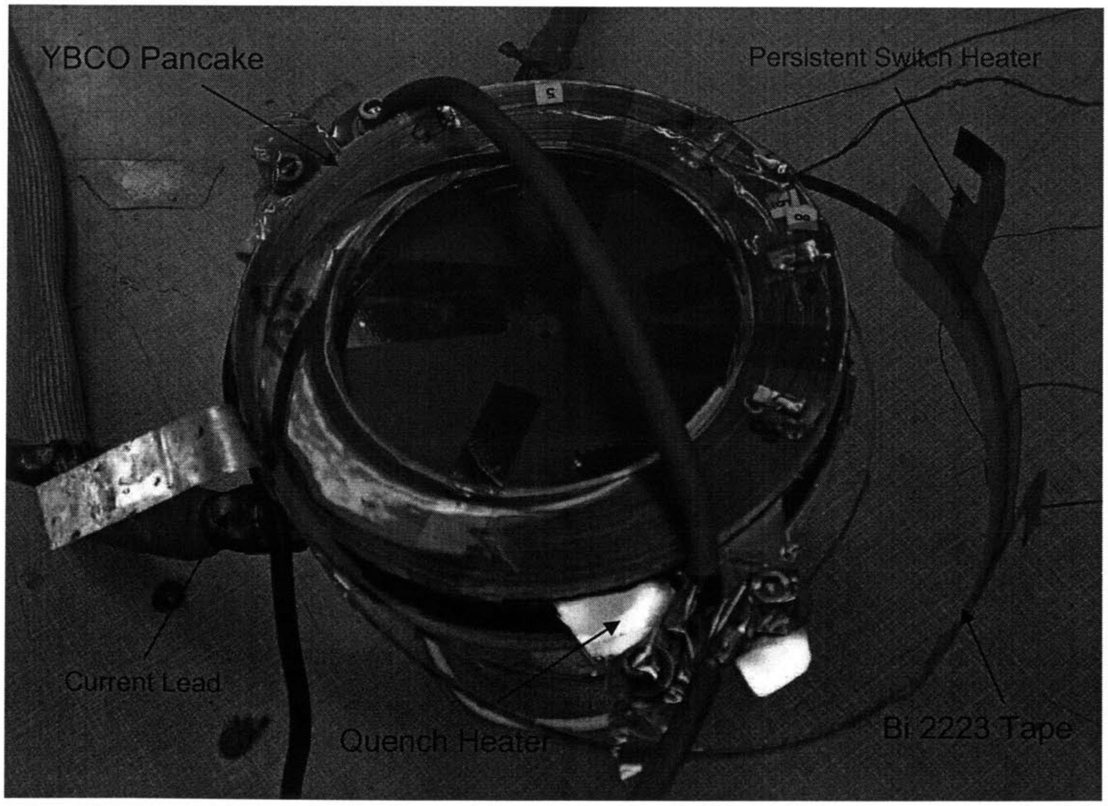

Figure 3.3.2c Top view of pancake coil

3.3.2(i) YBCO Coils and Voltage taps

Each coil was a single pancake wound with 20 m of YBCO tape with $I_c = 42$ A (77.3K) and index value of 15. The inner diameter of the coil was 7.5 cm and the outer diameter was 11.4 cm. Each coil had four voltage taps, with 6.66 m of tape between each tap. The two coils were connected with another YBCO tape, and were shunted with a Bi-2223/Ag tape that acted as a persistent switch.

From Figure 3.3.2b, it can be observed that the YBCO connection gives rise to the presence of a joint resistance between Tap 4 and Tap 5 (R_{joint1}), while the connection with the Bi-2223/Ag tape gives rise to joint resistances R_{joint2} and R_{joint3} between Tap 8 and Tap 1. The presence of these joint resistances causes the current in the persistent loop to decay – the loop current was not truly in persistent mode.

3.3.2(ii) Persistent Switch

As mentioned, the persistent switch (PS) was made out of strip of Bi-2223/Ag tape, with a resistance of 380 μΩ/cm at room temperature. A stainless steel heater was epoxied to the surface of the superconductor, with a type E thermocouple wedged between the heater and the superconductor. The thermocouple will indicate whether the switch is open during charge-up.

3.3.2 (iii) Quench Heaters

The heaters used to quench the YBCO coil was made of 78-μm thick stainless steel shim stock. The heater was shaped according to the surface of the coil, like a doughnut, and was epoxied to one surface of the coil. The heater had a resistance of 200 mΩ.

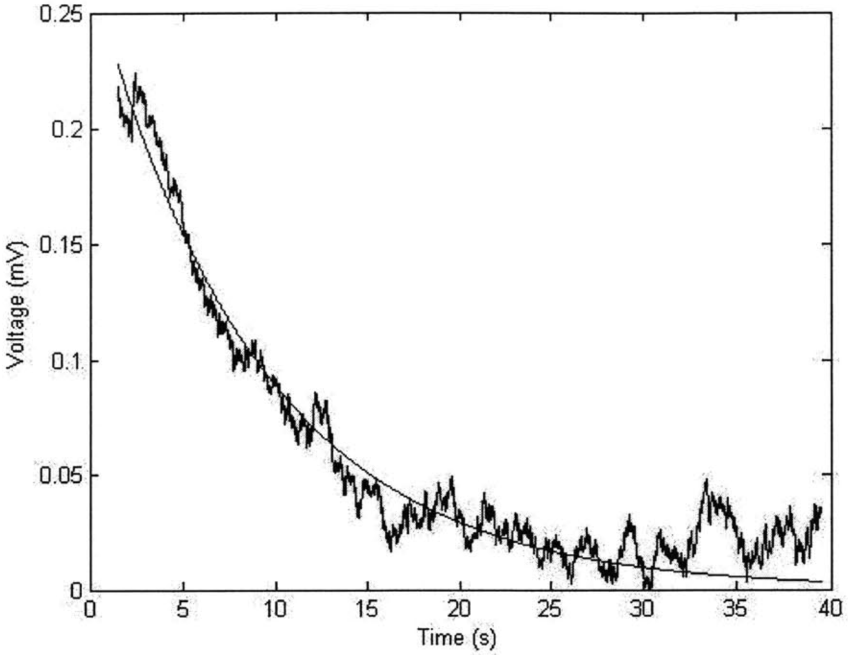

Figure 3.3.4(i)a Voltage profile recorded by Taps 4 and 5. An exponential fit was applied to the profile to enable the calculation of the total joint resistance in the coil.

The voltage profile can be calculate by the equation

$$V_{54} = R_{joint3} I_0 e^{-\frac{\sum R_{joint}}{L_{Tot}}t} - L_{50}\frac{dI}{dt}$$

Using FEMLab®, the mutual inductance of the coils can be calculated. The coupling coefficient is found to be 0.51. Therefore the total inductance of both coils, each with inductances of 690 μH, was then ~2.1 mH.

The regressive fit indicated that $V_{54} = 0.2716e^{-0.1119t}$, therefore,

$$\frac{1}{\tau} = \frac{\sum R_{joint}}{L_{Tot}} = 0.1119 \text{ s}$$

Hence, $\tau = 8.94$ seconds, and $\sum R_{joint} = 236$ μΩ.

3.3.3 Persistent Mode Operation

The coils were first put into "persistent mode" before the quenching process occurred. To put the coils in persistent mode, the persistent switch was kept resistive to allow most of the current from the power supply to flow into the coil. To do so, the PS heater was turned on and until the temperature of the Bi-2223/Ag tape recorded a temperature of ~140K, which was well above the critical temperature, T_c (~110K). After the PS became resistive, the current in the coils were increased until the targeted transport current was reached. After that, the PS heater was turned off to allow the PS switch to become superconducting again. The transport current from the power supply was shut off, and a current was induced in the persistent loop. The quenching of the YBCO coils was then initiated and the voltage from the taps was recorded on a LabView DAQ system.

3.3.4 Results

3.3.4(i) Characterization of Current Profile

From Equation 3.2c, $I(t) = I_0 e^{-\frac{t}{\tau}}$, we know that the presence of a resistance in the persistent loop greatly affects the rate of current decay in the loop. With the presence of the joint resistances, the current decay might be large enough that even before the coil is quenched, the current had fully decayed. At this point, an internal voltage would not be observed and the experiment would have failed.

Therefore, to quantify the total joint resistance in the loop, the coils were put in "persistence mode" with a transport current of 40A, and the rate of voltage decay was monitored. Taps 4 and 5 were used because the presence of the joint resistance allows a voltage to be recorded. Figure 3.3.4a presents the voltage profile from the joint. In the event that voltages from joint resistances are too small to be recorded, Hall probes can be used to measure the decay in the field.

The calculations indicate that the resistances in the coils are fairly high. The resistances could be the result of degradation in the tape caused by excessive heating during the soldering process, or could be due to a thick solder layer.

3.3.4(ii) Internal voltage with a transport current of 40A

In this particular run, the coil was set in persistent mode with a transport current of 40A through the coil. Immediately after the coil is put in persistent mode, the quench heater was initiated with a heating flux of 2 W/cm^2. The heating occurs and the voltage arising from the coil is recorded (see Figure 3.3.4(ii)a).

The figure shows how the voltage varies across the coil when the coil is quenched. The voltage profile matches the analytical approximation given in Figure 3.2b. As can be observed, V_{78} rises to a maximum of 16 mV. This indicates that the resistive voltage arises between these two taps because the weakest section is present in this region or that the heating is inhomogeneous over the coil. It can also be calculated that the sum of the voltage between taps 1 and 7 is equal in magnitude but opposite in sign to V_{78} as expected.

To obtain the voltage profile across the coil, as is seen in Figure 3.2c, the voltage across the coil was summed up at a certain instance in time during quenching. See Figure 3.3.4(ii)b for results, and also the 3-D plot of how voltage varied against time and the fraction of the total coil length.

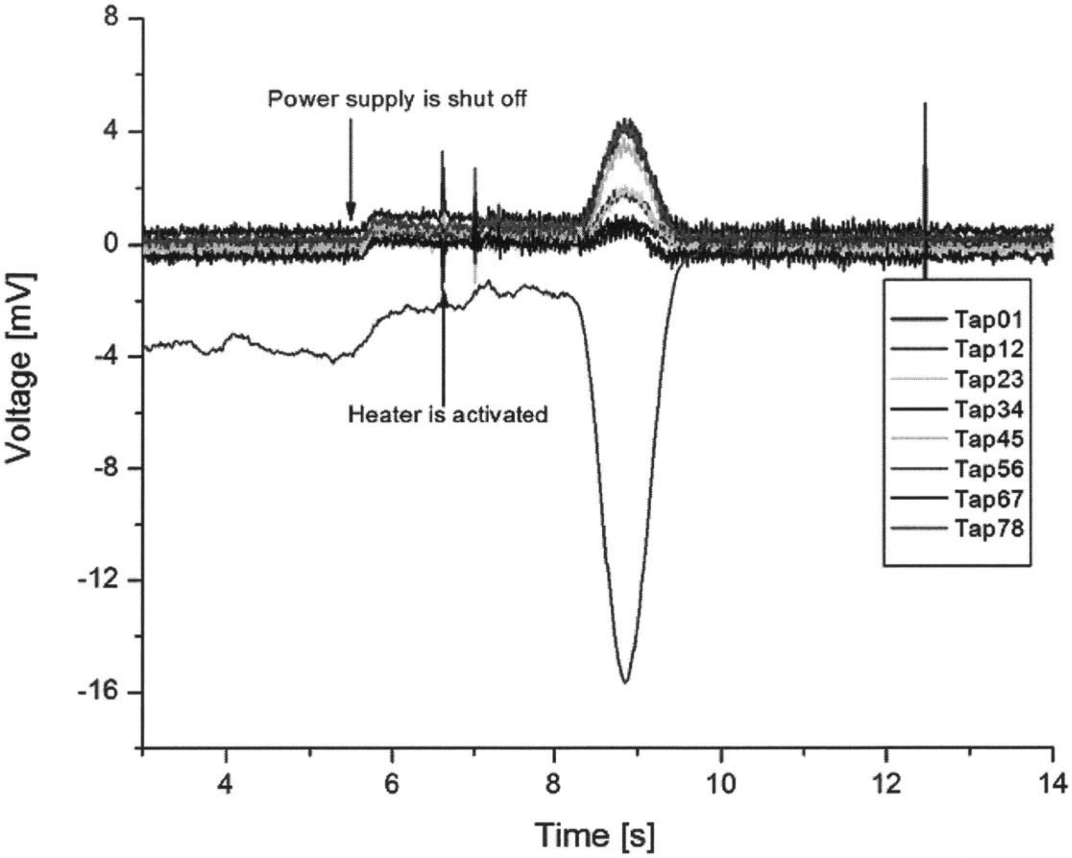

Figure 3.3.4(ii)a Voltage profile for quenching of a coil with a transport current of 40A

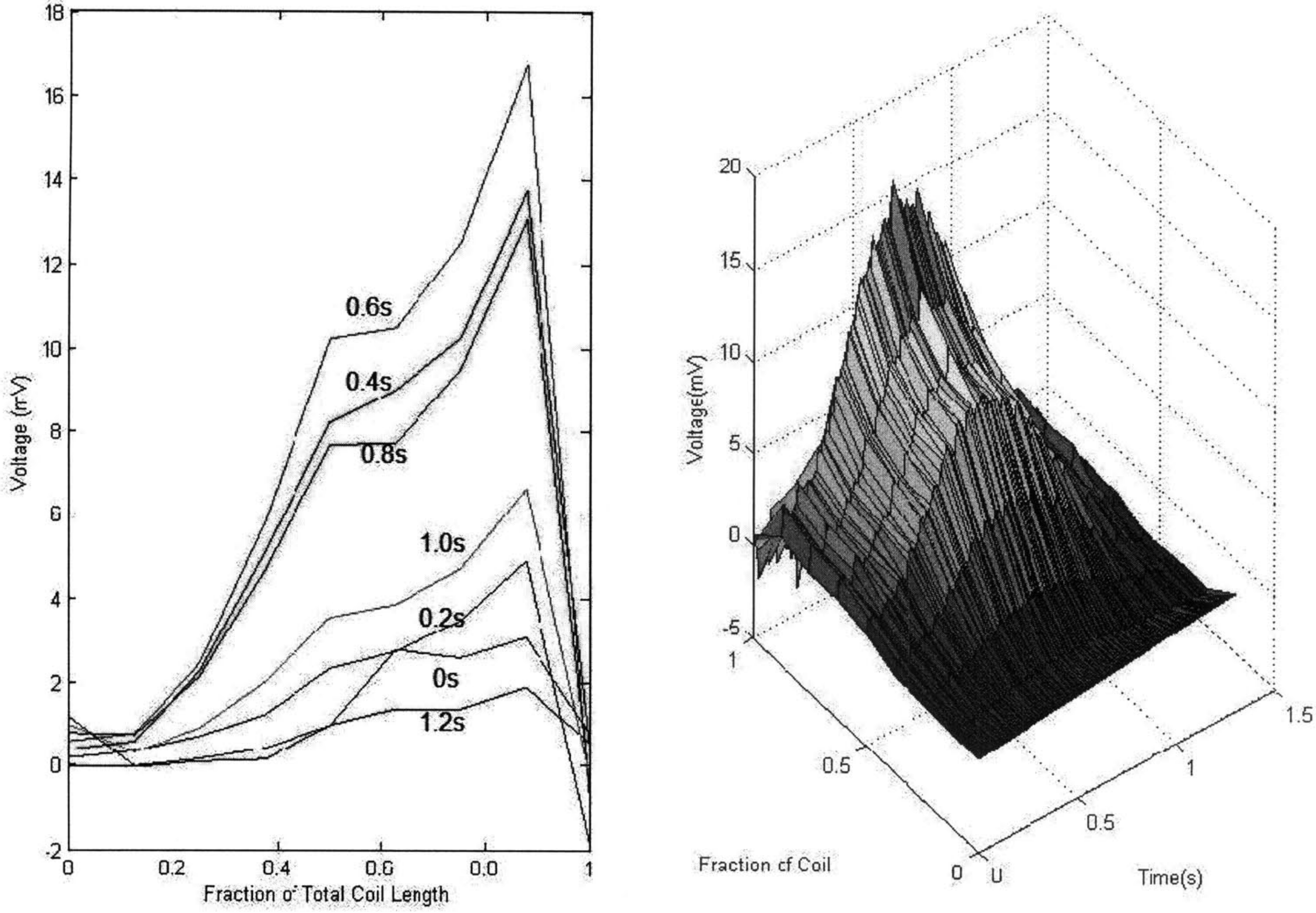

Figure 3.3.4(ii)b Variation of voltage across coil at certain instances of time starting from initial time at which quenching occurs (Left); 3-D plot of how voltage varies across coil length and time.

3.3.4(iii) Internal voltage with a transport current of 20A

The experimental procedure above was repeated with a transport current of 20A (app. 48% of I_c), instead of 40A. Since the current in the coil has decreased, it is expected that the internal voltage in the coil would be decreased as well. See Figure 3.3.4(iii)a for the plot indicating how the internal voltage varies across the coil during quenching, and how the internal voltage changes with time.

As can be observed, the resistive voltage occurs at the same section of the coil, creating an internal voltage of 10 mV, which lasts for a duration of approximately 1 second. The voltage profile is similar to that in Figure 3.3.4(ii)b because the resistance of in the coil rises in a similar fashion to that in 3.3.4(ii). This is because, the power density provided to the coil is the same. The voltage profile, its maximum and duration of the internal voltage is determined by the profile of the resistance increase in the coil.

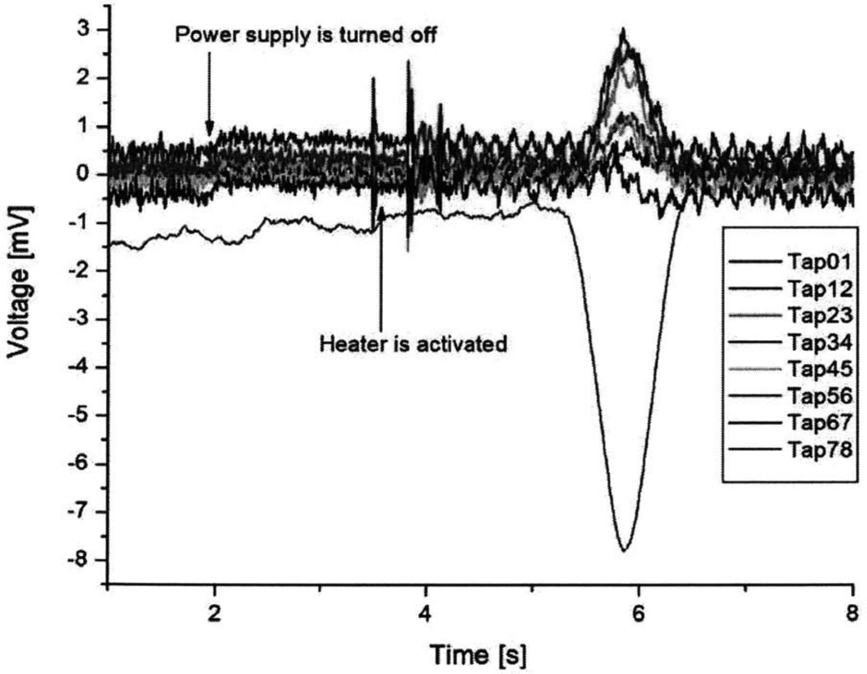

Figure 3.3.4(iii)a Voltage profile for quenching of a coil with a transport current of 20A

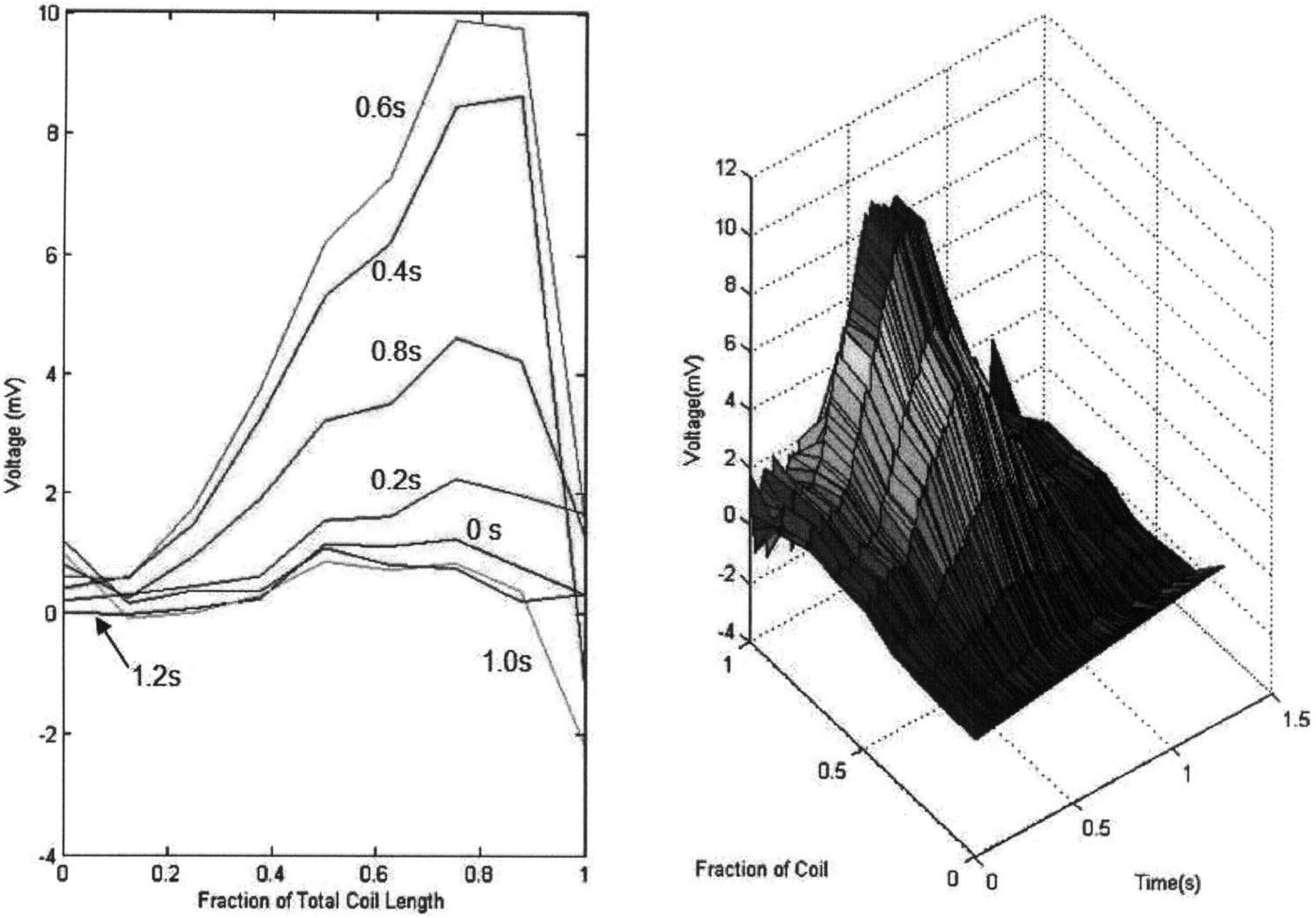

Figure 3.3.4(iii)b Variation of voltage across coil at certain instances of time starting from initial time at which quenching occurs (Left); 3-D plot of how voltage varies across coil length and time.

3.4 Numerical Simulation of Internal Voltage

To verify the results given in the sections above, a numerical simulation was written in Matlab® to simulate the occurrence of a quench in a given length of tape in a two coil assembly in persistent mode. In this simulation, a temperature profile was imposed on a given length of tape, *L*, and the variation of voltage across each pancake is observed when this tape quenches. The temperature profile imposed on the tape is obtained by solving the heat balance equation. Having obtained the temperature variation over time, the voltage rise in the tape can be calculated using a parallel resistance model. In the following sections, the theory will be explained in greater detail. Figure 3.4a gives a map of how the algorithm is performed, while the actual code is attached in Appendix IV.

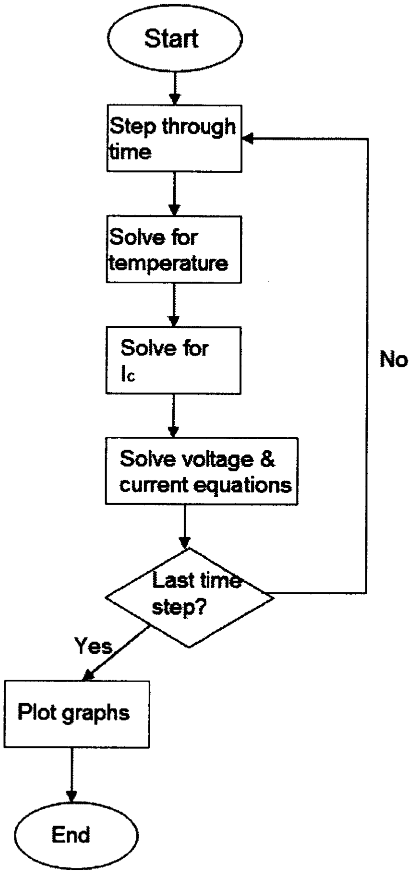

Figure 3.4a Basic architecture of how the internal voltage simulation algorithm is executed

3.4.1 Derivation of Temperature Function

As mentioned, the temperature of a section of tape with length, *L*, is modeled to rise homogenously as a constant heat flux, *q*, is input into the tape. Convection cooling through liquid nitrogen occurs at the edges exposed to the liquid. The effects of joule heating are also neglected because the heat input through the quench heaters are calculated to be three orders of magnitude larger than the joule heating. See Figure 3.4.1a for illustration of the heated section that is described.

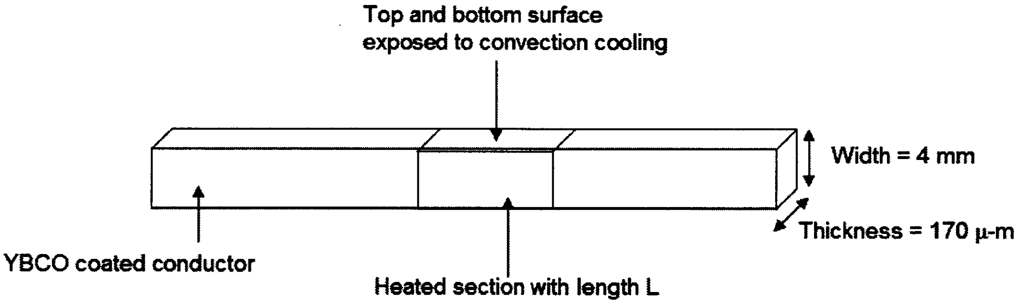

Figure 3.4.1a Illustration of heated section used in simulation

The heat balance equation used for this model is given by

$$C_{cd}V\frac{dT}{dt} = Q_{gen} - Q_{cooling}$$

$$C_{cd}\frac{dT}{dt} = q_{gen} - \frac{hA}{V}(T - T_o) \qquad (3.4.1a)$$

where h is the convection coefficient of nitrogen in the nucleate boiling phase, A is the surface area exposed to liquid nitrogen, and V is the volume of the tape. h is assumed to be constant since the temperature rise in the tape is assumed to be relatively small during the time in which the current fully decays in the loop.

To solve Eq. 3.4.1a, let $\theta = T - T_o$ and $\alpha = \frac{hA}{V}$,

$$C_{cd}\frac{d\theta}{dt} = q_{gen} - \alpha\theta$$

The solution is thus, $\theta = \frac{q_{gen}}{\alpha}\left(1 - e^{-\frac{\alpha t}{C_p}}\right)$ with the boundary condition that $\theta(0) = 0$. In terms of temperature, T, the equation is given as

$$T(t) = \frac{q_{gen}}{\alpha}\left(1 - e^{-\frac{\alpha t}{C_p}}\right) + T_o \qquad (3.4.1b)$$

With a heated length, L = 1m, and a heat generation of 1 W/cm^3, the temperature variation of the heated length of time is given in Figure 3.4.1a. As can be observed, the temperature rises from 77.3K to a maximum of 180 K in a little over 2 minutes. The heated input, q_{gen}, can be adjusted to increase or decrease the rate of temperature rise.

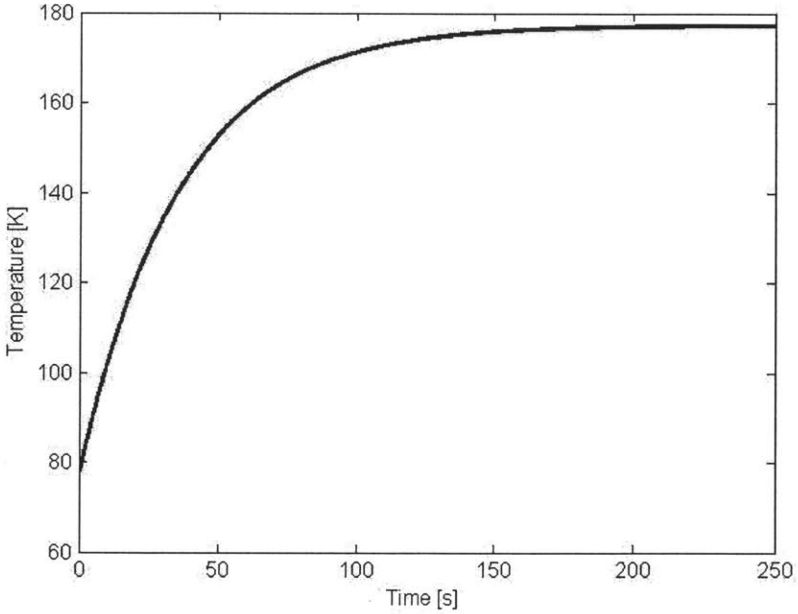

Figure 3.4.1b Variation of temperature of heated length with time.

3.4.2 Voltage Calculation

In this simulation, for a homogenous temperature rise in the heated length, the NZP velocity both in the longitudinal and transverse direction is assumed to be zero, even though in reality it is not likely to be true. Nevertheless, this assumption might not be as critical for HTS than in LTS because of its relatively low index number and small magnitude of stored energy in the magnet assembly. As was demonstrated in Table 2.2a, the longitudinal and transverse velocity for YBCO coil is ~4 mm/s and ~0.1 mm/s, which is relatively slow given the discharge time of the assembly on the order of 1-2 seconds for a 1 m heated length. Therefore, like the assumptions made in deriving the temperature profile, joule heating would not be a large factor that affects the voltage profile.

To model the voltage increase in the superconductor, a parallel resistance model is used, see Figure 3.4.2a. In the heated section, a resistance develops in the superconductor causing the current to divide into the copper/nickel matrix. The voltage generated by the current through the matrix, V_m, is equals to the voltage generated in the superconductor, V_s. We know that

$$V_m = I_m R_m \tag{3.4.2a}$$

$$V_s = V_c L \left(\frac{I_s}{I_c} \right)^n \tag{3.4.2b}$$

where V_c is the critical voltage criteria defined in this experiment as 1 μV/cm for a heated length, L; n is the index number of the superconductor; and I_c is the critical current at zero current density. Therefore, at all times, the condition $I_m R_m = V_c L \left(\frac{I_s}{I_c} \right)^n$ must hold true. The resistance across the superconductor, R_s, can be calculated as such

$$R_s = \frac{V_c L}{I_c} \left(\frac{I_s}{I_c} \right)^{n-1} \tag{3.4.2c}$$

Thus the effective resistance of the tape, R_{eff}, calculated using a standard parallel resistance equation is given as

$$R_{eff} = \frac{R_m R_s}{R_m + R_s} \tag{3.4.2d}$$

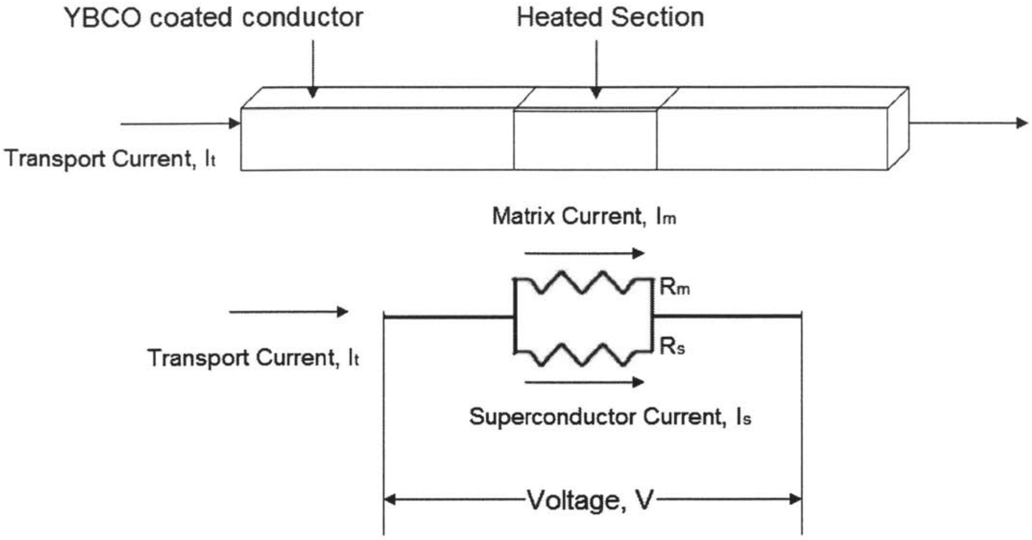

Figure 3.4.2a Parallel resistance model used in numerical simulation

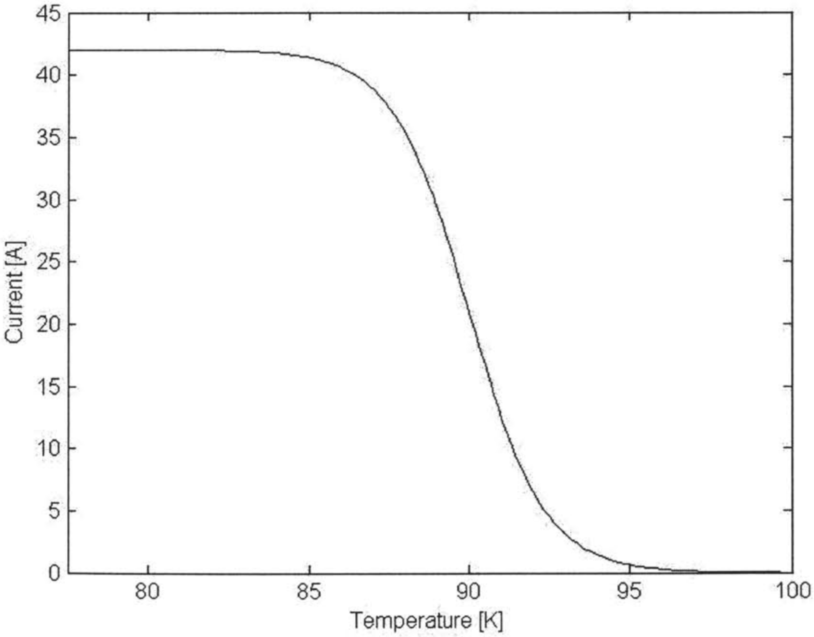

Figure 3.4.2b Variation of critical current, I_c, with temperature, T used in simulation.

The voltage in the superconductor is affected by the temperature through the critical current, I_c. In the model, the function represented in Figure 3.4.2b was used to trace the variation of I_c according to T. The function used to describe I_c is:

$$I_c(T) = \frac{I_{crit}}{\left(1 + e^{\frac{T - T_{cs}}{\kappa T_c}}\right)} \qquad (3.4.2e)$$

where I_{crit} is the critical current at $T = 0$ K, and κ is a constant used to characterize the curve. A particular advantage of using this function over the typical linear approximation curve is that discontinuities close to the critical temperature can be avoided.

Lastly, for a current loop in persistent mode, the inductive voltage generated across the coils should be equal and opposite to the resistive voltage generated during a quench. The inductive voltage, $V_L = (L_1 + L_2 + 2M_{12})\frac{dI(t)}{dt}$. Therefore, at every time step, a system of equations where

$V_L = V_m$ --------*(1)*

$V_L = V_s$ --------*(2)*

$I_t = I_m + I_s$ -----*(3)*

needs to be solved simultaneously. Essentially, there are three equations and three unknowns, namely I_t, I_s and I_m that needs to be solved for.

3.4.3 Simulation Results

The numerical simulation was used to verify the experimental results given in Section 3.3.4(ii) with a heated tape length of 1 m. In the simulation, only the voltage across each of the two coils is monitored as opposed to segmenting each coil into three sections like what was done in the experiment. Therefore, to compare the experimental and simulated results, the voltages in the experiment would have to be summed across four taps.

With an initial charge-up current of 40 A, the model yielded internal voltages that were much higher than were observed in the experiment. The simulation was adjusted until a transport current yielded results that were close to the experimental results. Since current was not measured in the experiment, it became a parameter that the simulation can elucidate.

With a transport current of 12.5 A, it is discovered that the simulated voltage matches very well with the experimental results. The simulated results are overlayed on top of the experimental results in Figure 3.4.3a. As can be observed, even the inductive voltage generated on in Coil 1, namely V40, before the quench (when the time is less than 2 seconds) matches well with the simulated results.

The variation of the current and resistance corresponding to the voltages are also plotted in Figure 3.4.3b and Figure 3.4.3c. It can be observed that the transport current decays before the quench because of the presence of the joint resistances. During the quench, the current decays rapidly, dividing into the matrix as the superconductor resistance rises rapidly. The matrix resistance is assumed to be constant during that time frame, and as can be observed, the effective resistances of the tape, R_{eff} rises along with the superconductor resistance during the quench.

Finally, in Figure 3.4.3d, the temperature profile of the tape is given. The temperature of the tape rises from 77.3 K to a maximum of 97 K, which is above the critical temperature. Since the time length needed to fully discharge the coil is relatively small, the temperature variation resembles a linear function. Since the temperature rise is only ~15K, before the transport current decays fully, the assumptions that assume constant convection coefficient, h, and constant resistivity properties in the matrix, are justified.

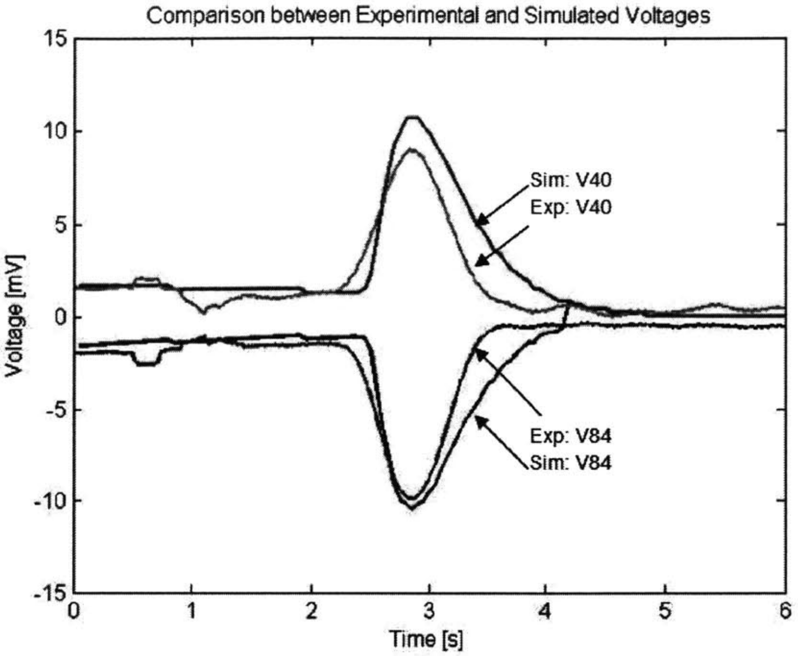

Figure 3.4.3a Simulated and experimental results from Section 3.3.4(ii)

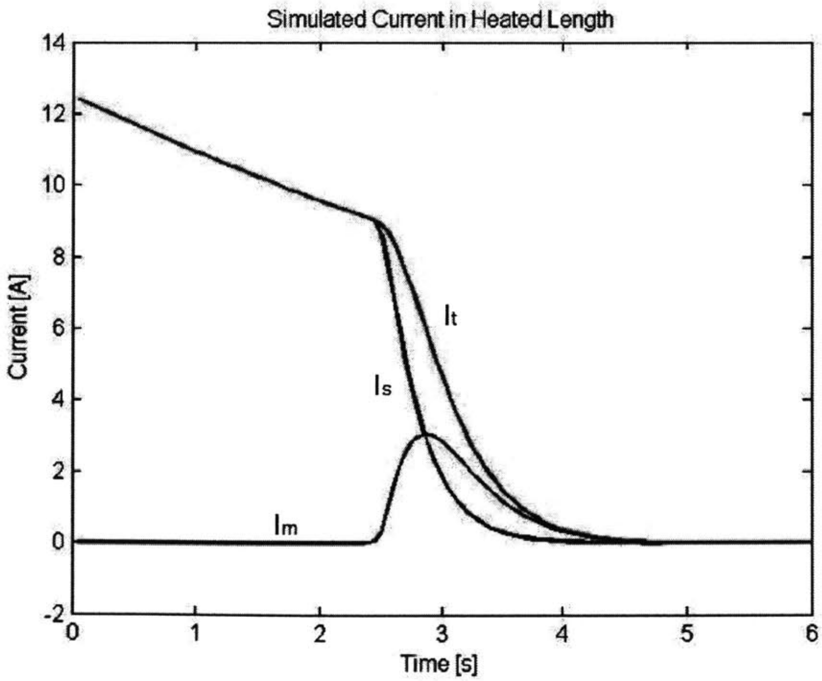

Figure 3.4.3b Simulated profile of currents in the heated length. I_t corresponds to the total current, while I_s and I_m correspond to the currents in the superconductor and matrix.

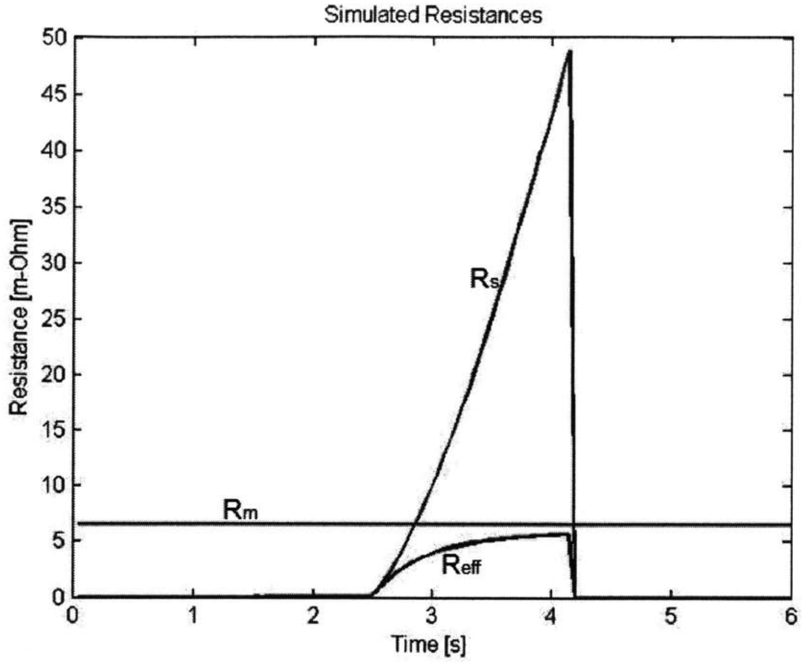

Figure 3.4.3c Simulated resistances in the heated length. R_s and R_m correspond to the resistances in the superconductor and matrix, while R_{eff} is the effective resistance.

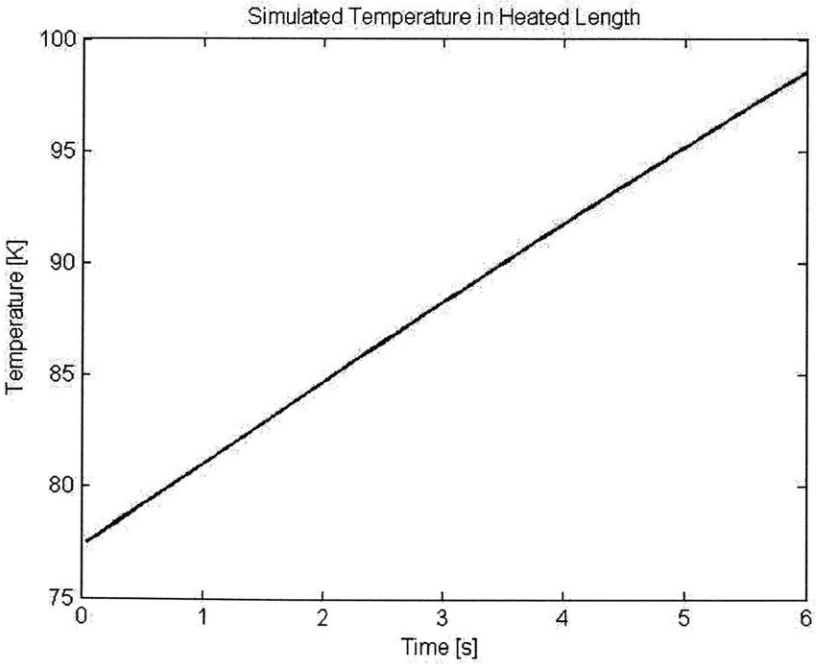

Figure 3.4.3d Simulated temperature profile in the heated length

3.4.4 Discussion

The simulation results indicated that the current induced in the magnet during the charge-up phase is much smaller than expected. This can be attributed to losses incurred through the persistent switch. It should be noted that the energy loss, E_R, is given by Wilson [5] as:

$$E_R = \frac{2E_oL}{RT}$$

where E_o is the energy stored in the magnet, L is the total inductance, R is resistance of the persistent switch when it is turned on, and T is the time taken to charge magnet up. In this experiment, the resistance of the BSCCO tape used in the persistent switch is relatively small, $R \sim 1\ \text{m}\Omega$. Therefore, if the time to charge-up the magnet was on the order of ten seconds, the fractional loss, $\frac{E_R}{E_0}$, would be approximately 40%, which is very significant. Therefore, the persistent switch should have a larger resistance, or the charge-up time should significantly be increased to reduce loss in the switch.

Using the simulation, the effects of the heated lengths, L, on the maximum internal voltage, with a given heat input, q_{gen}, was also studied. Using a transport current of 40A, with no joint resistances, and with a heat input of 6 W, the variation of internal voltage with respect to heated length is given in Figure 3.4.4a. As can be observed, as the heated length increases, the maximum voltage in the coil decreases. This is because as heat is distributed over a longer length of tape, the resistance in the coil rises at a more gradual rate, discharging the stored energy gradually. This has implications for the passive protection technique described in Chapter 2; namely spacers that can dissipate thermal disturbances quickly can also minimize the occurrence of hot spots in magnets. In addition, it also implies that active protection techniques that increases the fraction of the normal section during a quench would have positive effects on reducing internal voltages.

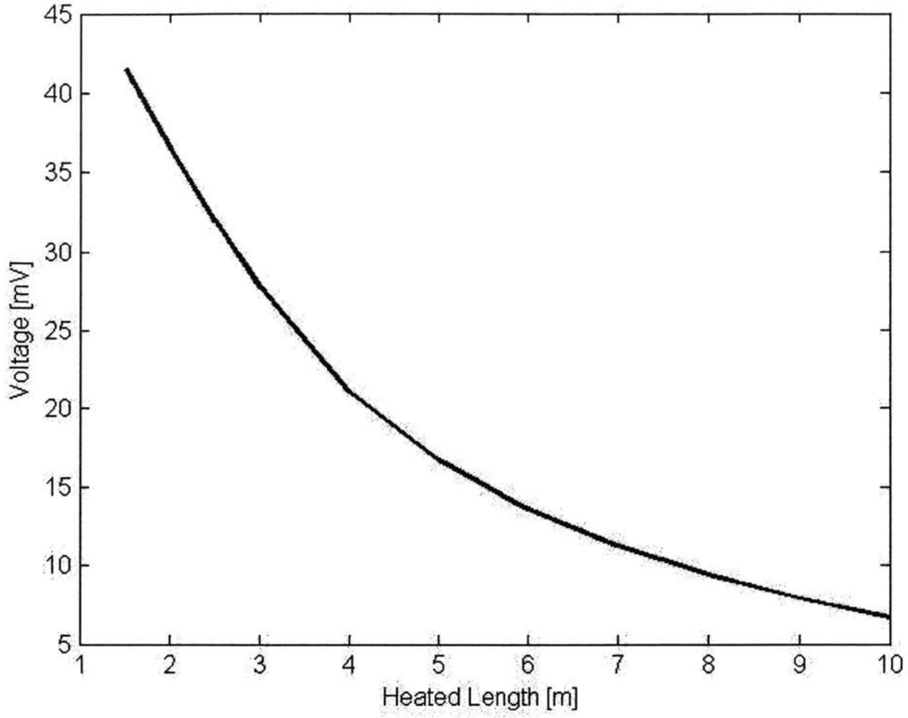

Figure 3.4.4a Variation of internal voltage with heated coil length, given a heat input of 6 W for the simulated experimental coil of 2.1 mH and zero joint resistance

3.5 Chapter Summary

In this chapter, the phenomenon of internal voltage was derived analytically and observed experimentally on a small test coil assembly put in persistent mode. Internal voltage occurs because of the interaction between the inductive voltage and resistive voltage during a quench. Particularly in large magnets where the inductance of a coil gets large, the time constant $\left(\frac{L_{Tot}}{R(t)}\right)$ for the current in the coil to decay increases, and a potentially damaging internal voltage could develop in the coil.

A simulation was written to validate the experimental results. From the simulation it was inferred that the induced current was smaller than expected. Nevertheless, the simulation matched well with experimental results. Finally, the simulation also showed that during a quench, when a quench section is enlarged, internal voltage can be reduced.

Chapter 4- Acoustic Emission

4.1 Introduction and History

Acoustic emission (AE) relates to the generation of stress waves or acoustic pressure resulting from vibrations induced by energy releasing processes such as fractures, friction, motion and so forth. AE sensing, on the other hand, relates to the use of piezoelectric devices to detect a cracking event that induces pressure waves. AE sensing is widely used in commercial applications to detect stress corrosion, fatigue cracking, crack propagation, and leak occurrences.

AE sensing has been used in superconducting magnet applications since the early 1980's [10] [15] [16], in LTS applications to detect conductor motion and mechanical disturbances that initiate a quench in the magnet. Figure 4.1a illustrates the outputs for two AE sensors on a dipole magnet during a quench caused by conductor motion [10]. The voltage spike indicates the time at which the quench is induced and the corresponding signal obtained from the AE sensors.

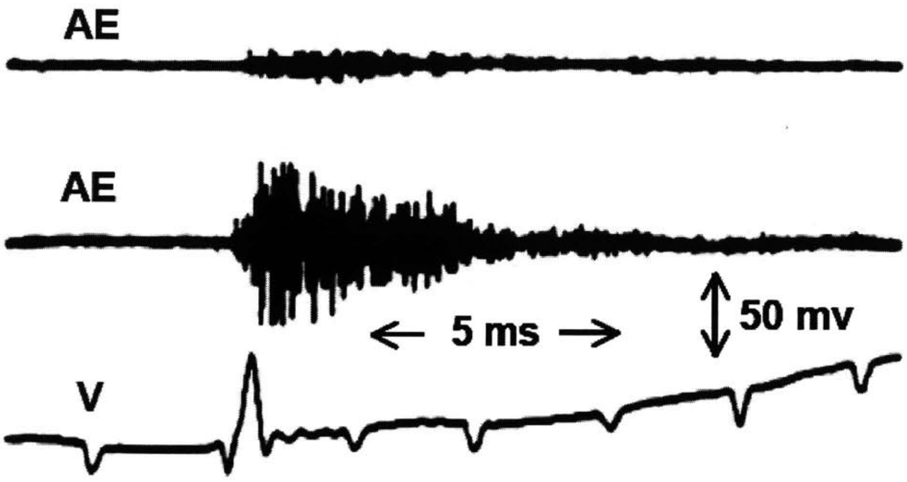

Figure 4.1a AE signals obtained during the event of a quench caused by conductor motion in a dipole magnet. [10]

4.2 AE in HTS

It is generally agreed that HTS is much more stable than LTS; HTS magnets will not quench from a disturbance caused by conductor motion or epoxy cracking. However, HTS remains susceptible to permanent damages by overheating, which to date, is detected through voltage measurement.

Because non-uniform overheating within the winding of a magnet induces thermal stresses and strains, in principal AE signals should be generated during a quench. It should be noted that AE signals would arise only during transient heating because AE signals are caused only by time-varying stresses. In steady state, microcracks and creep would generally occur at extremely small rates.

Lee *et al* [4] applied AE to detect hot spots in HTS coils operating at the boiling temperature of liquid nitrogen (77.3 K). They detected significant AE signals in a double pancake coil wound with Bi-2224/Ag tape by heating a small section of the pancake with a heater. The minimum level of overheating for AE detection was about 3 K. The results paint a promising future for the use of AE as a complement to the use of voltage taps in the detection of overheating in an HTS coils. In the following sections, an experiment will be conducted to verify their findings and to elucidate more on AE generation in a hot spot.

4.3 Sensor Assembly and Instrumentation

As stated above, AE sensors rely on piezoelectric effects in which strains in certain crystals, such as quartz, produce electric potential. The sensors used in this project are custom-made at the FBML, and can withstand applications at cryogenic temperatures. The sensors are of the differential type comprised of two halves of a sensor disk placed in opposite polarities. The differential sensor doubles the voltage output while canceling electrical noise. Figure 4.3a presents an illustration of a sensor.

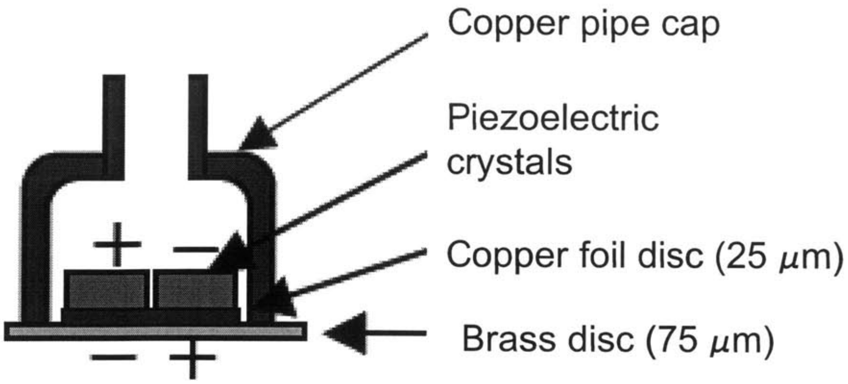

Figure 4.3a AE sensor assembly. Width of the sensor is ~10 mm. [5]

The AE sensor produces high-frequency signals on the order of hundreds of kHz, while its amplitudes are as low as microvolts. Given the magnitude of its signals, a preamplifier (Physical Acoustic Inc.) is used to increase the signal-to-noise ratio before the AE signals are recorded. The amplification used in this project is 40 to 60 dB. The output is then recorded on a digital oscilloscope with a sampling frequency greater than 1 MS/s. Figure 4.3b presents a block diagram of the AE instrumentation system used.

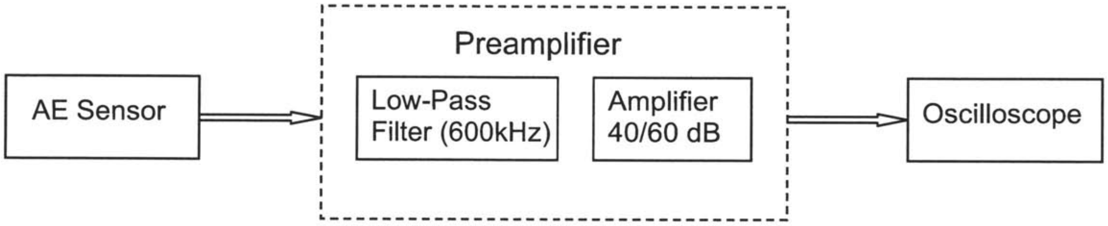

Figure 4.3b Instrumentation system for AE signal detection

4.3.1 Oscilloscope

Due to the high frequency of AE signals, care has to be taken when discrete sampling is applied in the recording of AE waveforms. Two important parameters for selecting a proper oscilloscope are i) sampling rate, and, ii) data storage capacity.

In order to obtain the correct waveform from the AE signal, the sampling rate has to be greater than twice the Nyquist frequency – the maximum frequency to be sampled. In this case, the sampling rate needs to be greater than 1 MS/s.

When a high sampling rate is used, data storage could potentially limit the amount of recording time. For our experiment, a Yokogawa, DL 750P ScopeCorder, with a maximum sampling frequency of 10 MS/s and 1 Gigabytes of hard disk space was used. At the maximum sampling rate, approximately 100 seconds of data can be recorded.

4.4 The Kaiser Effect

An important phenomenon that needs to be noted during repeated uses of AE monitoring is the Kaiser effect. The Kaiser effect occurs when a material under stress emits pressure waves only after the previous load level is exceeded. During repeated trials, a material is 'trained' and AE signals that are previously recorded diminish with the number of trials. Therefore, it should be noted that repeatability of an experiment might be affected by such phenomena.

4.5 Experiment I – AE Detection on a Single Strip BSCCO Tape

4.5.1 Overview

The focus of this experiment was to obtain and characterize AE signals during the heating of a BSCCO-2223 tape in liquid nitrogen (77 K) conditions. A trapezoidal temperature profile, whereby a section of the BSCCO tape undergoes transient heating, steady-state heating and then transient cooling, is used to induce stresses that create AE signals. In addition, the minimum temperature rise that was needed to consistently produce the signals was also investigated.

4.5.2 Experimental Setup and Procedure

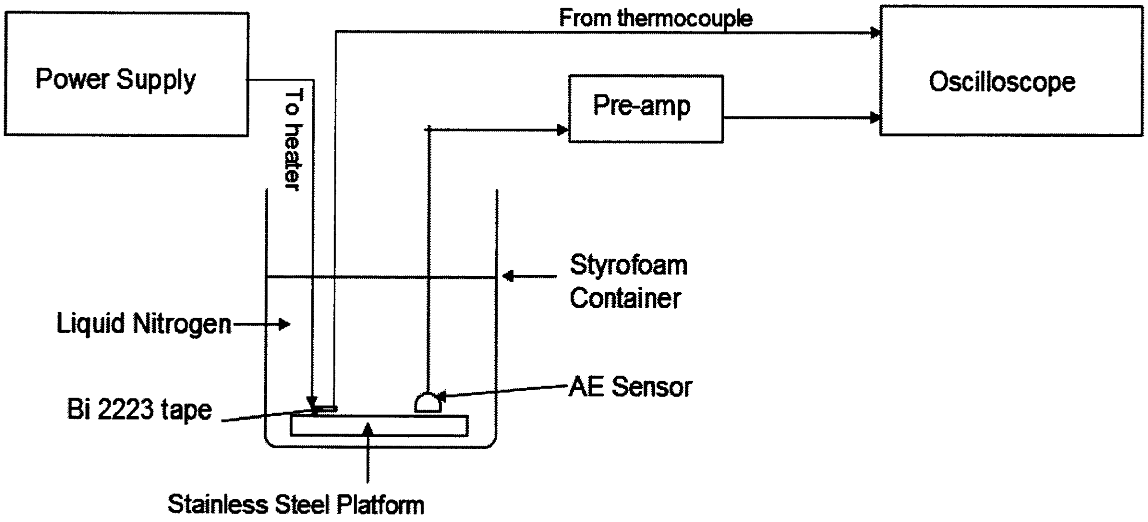

Figure 4.5.2a Schematic drawing of the experimental setup

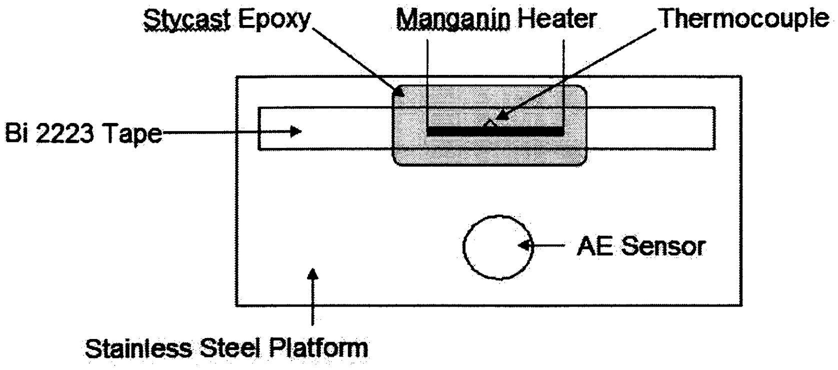

Figure 4.5.2b Schematic drawing of the top view of the steel platform (~10 cm) with the Bi-2223 tape and AE sensor.

Figure 4.5.2a shows a schematic drawing of the overall experimental setup. The BSCCO tape (I_c>100A at 77.3 K), approximately 10-cm long, was mounted onto a steel platform, with the AE sensor attached ~2 cm away on the same planar surface, as shown in Figure 4.5.2b. A manganin heater, attached to the surface of the BSCCO tape with Stycast® epoxy, was used to heat the tape. During transient heating, AE signals will be recorded on the oscilloscope.

The experiments were conducted without a transport current through the tape. The heater was activated using step currents with heat inputs up to 16 W for 7 to 10 seconds. The sampling rate of the oscilloscope is set at 2 MS/s. Using an FFT of the signals produced from an AE sensor, we determined the maximum signal frequency to be 500 kHz. Therefore, the sampling rate of 2 MS/s should be sufficient to obtain all signals without aliasing the signals.

4.5.3 Results

As shown in Figure 4.5.3a, significant AE signals were obtained at the initiation of the heating, with a few more spikes during heating and additional events during cooling after the heating is removed. The two spikes observable on the temperature profile correspond to inductive voltage surge during the turning on and turning off of the heater current supply and can be used to indicate when heating starts and ends. The AE signals are believed to be caused mainly by the thermal expansion in the Stycast® epoxy which has a relatively a high linear thermal expansion coefficient, in comparison to the materials in the tape (see Table 4.5.3a). Therefore, microslips and cracking are prone to occur in the epoxy because a large temperature gradient induces large strains within the epoxy. It should be noted that for an unconstrained body, strain in any direction, ε, due to heating is given as

$$\varepsilon = \alpha \Delta T$$

where α is the coefficient of thermal expansion, and, ΔT is the change in temperature. The time variation of strain, which is believe to generate AE, assuming α is constant, is thus given as

$$\frac{d\varepsilon}{dt} = \alpha \frac{dT}{dt}$$

Obviously, from Figure 4.5.3a, this rule is not strictly adhered to because AE signals are not detected even when there is a small variation in temperature. However, the equation does indicate with a large temperature gradient, strain increases, and therefore AE signals are generated as well.

Table 4.5.3a Linear thermal expansion coefficient of various materials at 77 K

Material	Linear Thermal Expansion Coefficient at 77 K (x10^{-6})[K^{-1}]
Stycast® epoxy	29
Copper	17
Nickel	13
Manganin	10
Stainless Steel	17.3
Nomex	20

The results, however, indicate that AE signals may be detectable during the initiation of a hot spot. What remains unclear, however, is the origin of the signals; the signals generated from the layer of Stycast® epoxy in the sample holder are not the same as those that might be generated by a hot spot in the superconductor. The results would not necessarily indicate that the AE technique is applicable in detecting hot spot and quench occurrences in real coil assemblies.

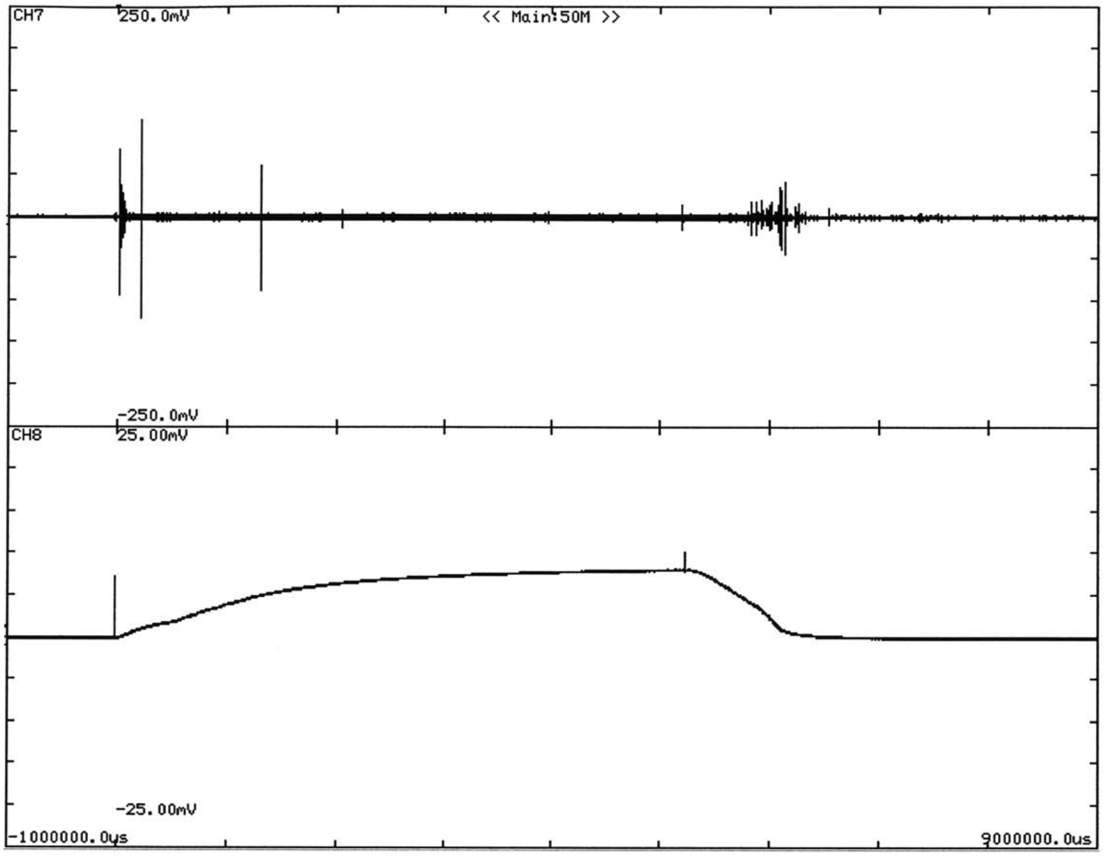

Figure 4.5.3a (Top) AE signal; x-axis scale: 1 s/div, y-axis scale: 50 mV/div; (Bottom) Temperature profile from thermocouple; x-axis scale: 1 s/div, y-axis scale: 5 mV/div, with the maximum temperature being ~290K (~10 mV).

To achieve the second objective of this test, which is to find a minimum ΔT for which AE signals can be consistently detected, the heat input through the heater was varied. At a ΔT of ~4 K, AE signals were observed during the first two runs of the test but not for the subsequent ones. This phenomenon can be attributed to the Kaiser effect whereby the AE effect decreases with repeated runs of the experiment. The minimum ΔT for which AE signals consistently occurs is at 10 K. In repeated runs of the test (approximately 20 times), signals were observed for all the runs. A typical trace of a run is given in Figure 4.5.3b, while Figure 4.5.3c shows a detailed profile of the large AE spike that occurs at t= 0.997 s from the start of heating.

Figures 4.3.5b and c indicate that AE was generated when the temperature rise in the thermocouple was about 7K above 77K. The signal in Figure 4.3.5c is similar to the signal shown in Figure 4.1a, which was due to conductor motion. The duration of a signal is approximately 5 ms, and the maximum amplitude of the signal prior to amplification is 8 μV.

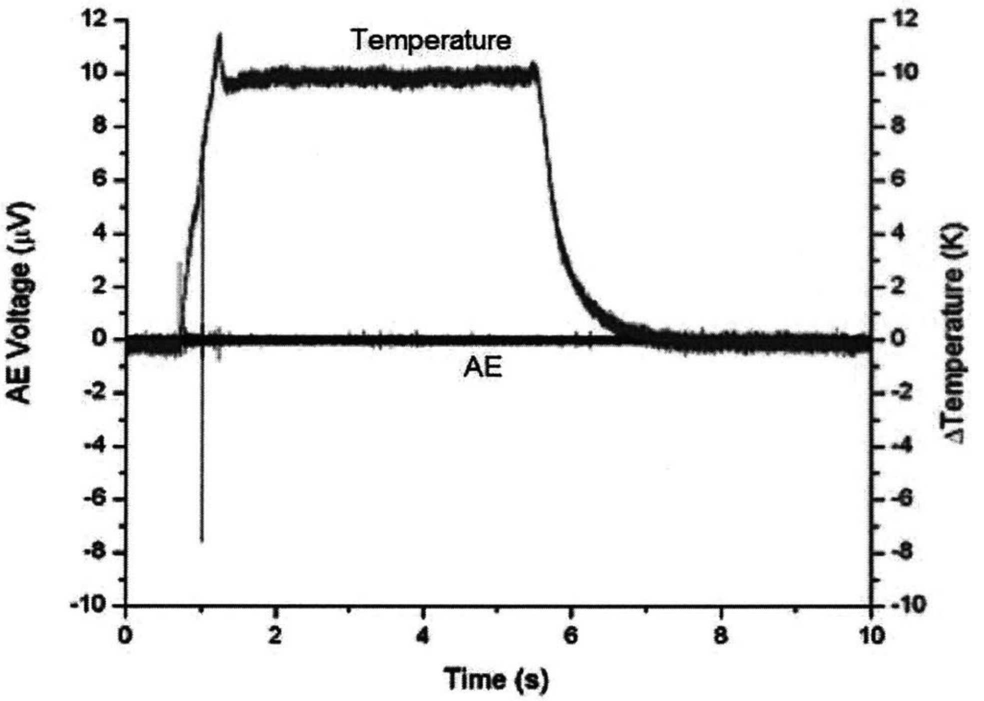

Figure 4.5.3b Temperature and AE traces for ΔT of 10 K

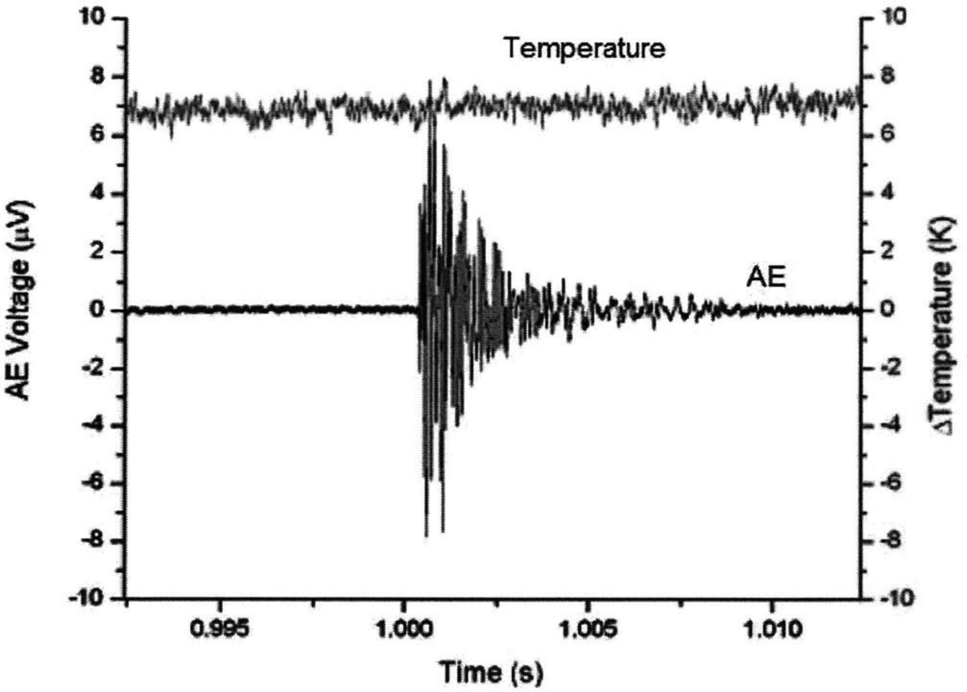

Figure 4.5.3c Amplified view Figure 4.5.3a where AE signal is captured

4.5.4 Conclusion

Results have indicated that a temperature increase of ~4 K in this setup is sufficient to generate AE signals. However, this effect cannot be sustained due to the Kaiser effect and, hence, subsequent runs yield no noticeable signals. For a temperature increase of ~10 K in the tape, AE signals were obtained for most trials.

The experiment has demonstrated that the thermal stresses and strains caused by the expansion rates of different materials during a heating process create AE signals. However, a very fundamental question that this setup has failed to answer is the origin of the signal i.e. whether it originated from the Bi-2223 tape or from the epoxy. Ideally, AE signals should originate from within the coil winding to simulate an actual quench event.

4.6 Experiment II – AE Detection on a Single Pancake YBCO Coil

4.6.1 Overview

In this experiment, a single pancake YBCO coil was used to test the ability of the AE sensor to detect the inception of a quench event, if possible, before detection by voltage signals. The coil, with the sensor, is submerged in liquid nitrogen and the coil is quenched via a manganin heater attached to the inner diameter of the coil. A step heater current is input into the current-carrying coil to quench the coil and induce a thermal runaway. During this quenching process, the AE sensor is monitored to observe whether signals are generated. See Figure 4.6.2a and 4.6.2b for an illustration of the setup.

4.6.2 Experimental Setup

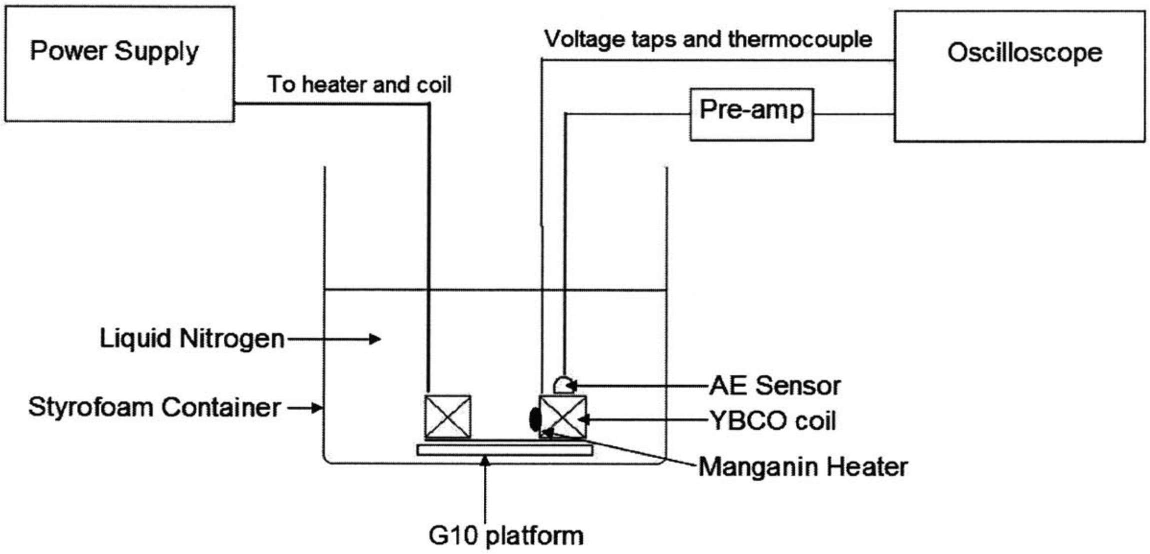

Figure 4.6.2a Schematic drawing of experimental setup for AE detection on a single pancake YBCO coil

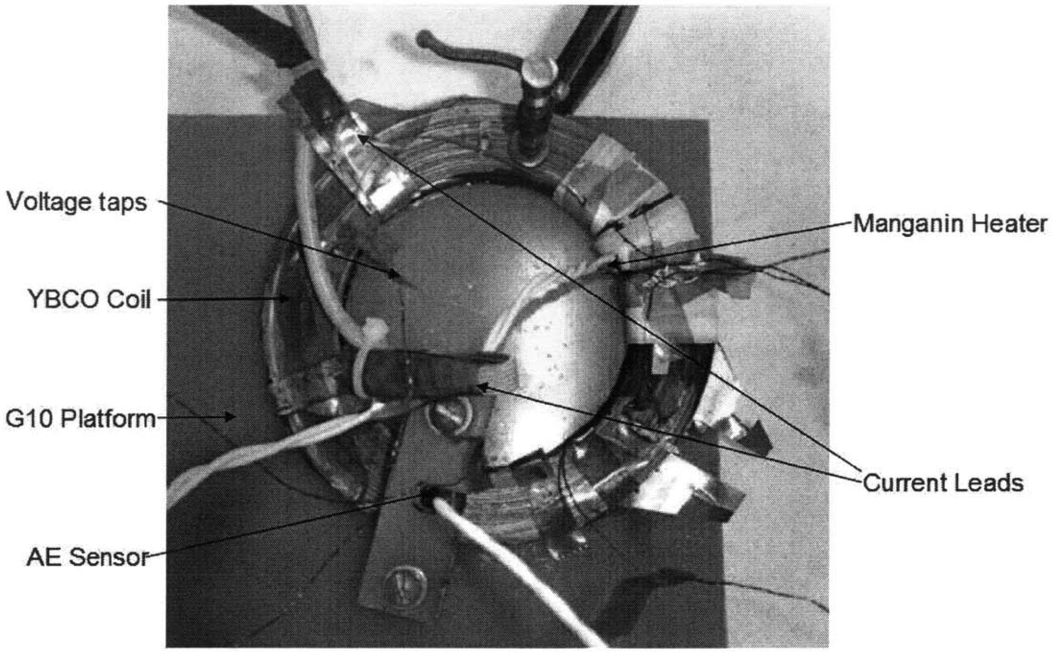

Figure 4.6.2b Top view of setup

4.6.3 Results

With a transport of 39 A (95% of I_c), and a heat pulse of 5 seconds, the coil was driven normal. Figure 4.6.3a shows the variation of the voltage across the coil and the thermocouple voltage right at the point of the heater. It can be observed that the coil voltage rises as the heater is turned on, and after the heater is shut, a thermal runaway occurs because of joule heating in the tape. The voltage across coils also rises as the normal zone propagates both longitudinally and transversely through the coil. As can be observed from the figure, AE signals are recorded when the coil voltage reaches approximately 2 v. Obviously, this result is not acceptable for AE to be used as a quench detection device. Ideally, AE signals should be recorded as soon as quenching occurs, when the voltage across the coil is in the order of a few millivolts.

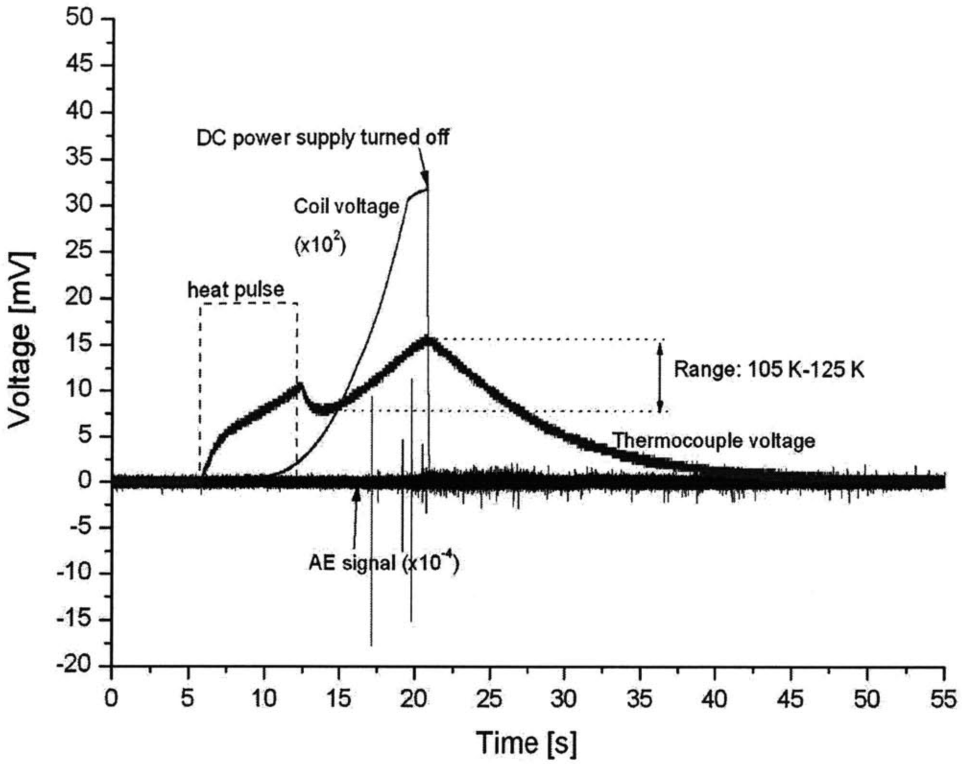

Figure 4.6.3a AE signals generated from the quenching of a single pancake YBCO coil

The test was repeated in the same conditions with a transport current of 39A, in liquid nitrogen conditions. Figure 4.6.3b shows a close up image of the AE signals generated during the quenching of the coil. The trigger level for AE signals in this case was set at 10 nV, which is the order of magnitude of the voltage generated from the AE sensor before pre-amplification. As can be observed from the figure, AE signals are generated at time = 0.63 s, which corresponds to a coil voltage of greater than 0.5 v. Again, it is observed that the AE signals do not precede the voltage signals; hence, AE does not appear to be very promising in detecting a quench event before it is detected by voltage signals.

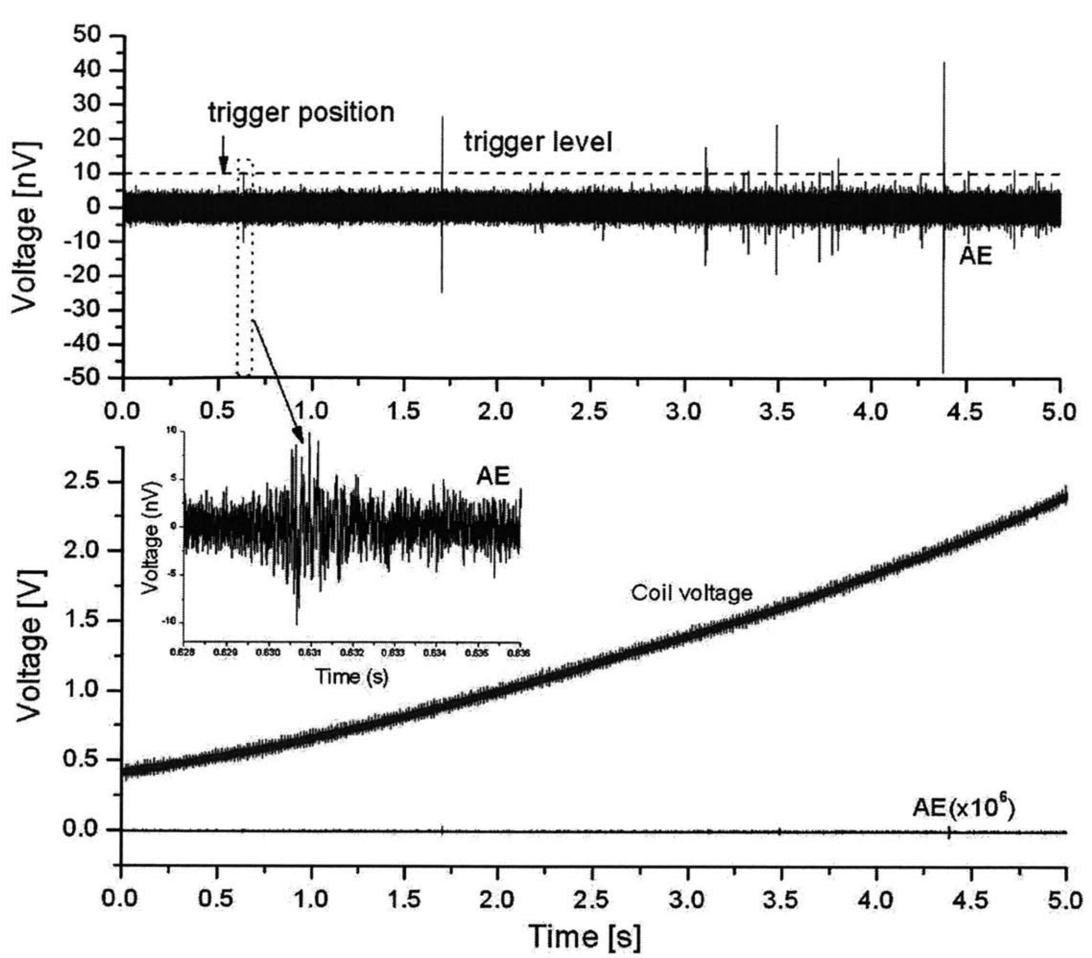

Figure 4.6.3b Coil voltage and AE signals generated for the quenching of a single pancake YBCO coil

As was noted in 4.5 Experiment I, AE signals could be generated from thermal strains induced in the heater or, more likely, Stycast® epoxy. Therefore, it is a noteworthy endeavor to determine if the AE signals generated from Figures 4.6.3a and 4.6.3b can be generated without any transport current, as was shown in 4.5 Experiment I. Figure 4.6.3c shows two runs of the experiment where the coil was heated without a transport current, and the first AE signals that had amplitudes above the trigger level. As can be observed, in the first case, the thermocouple temperature located at the site of the manganin heater, recorded a temperature of 91 K. In the second case, a temperature of 155 K was recorded. At both times, AE signals were generated when the coil was subjected to similar conditions, e.g. same heater currents, surrounding temperatures and so forth. It can then be concluded that the AE signals could be generated either with or without a coil actually quenching. However, since AE signals can be generated also at various heating temperatures, repeatability of these tests becomes an issue. Again, the Kaiser effect might play a significant role in determining the repeatability of the results.

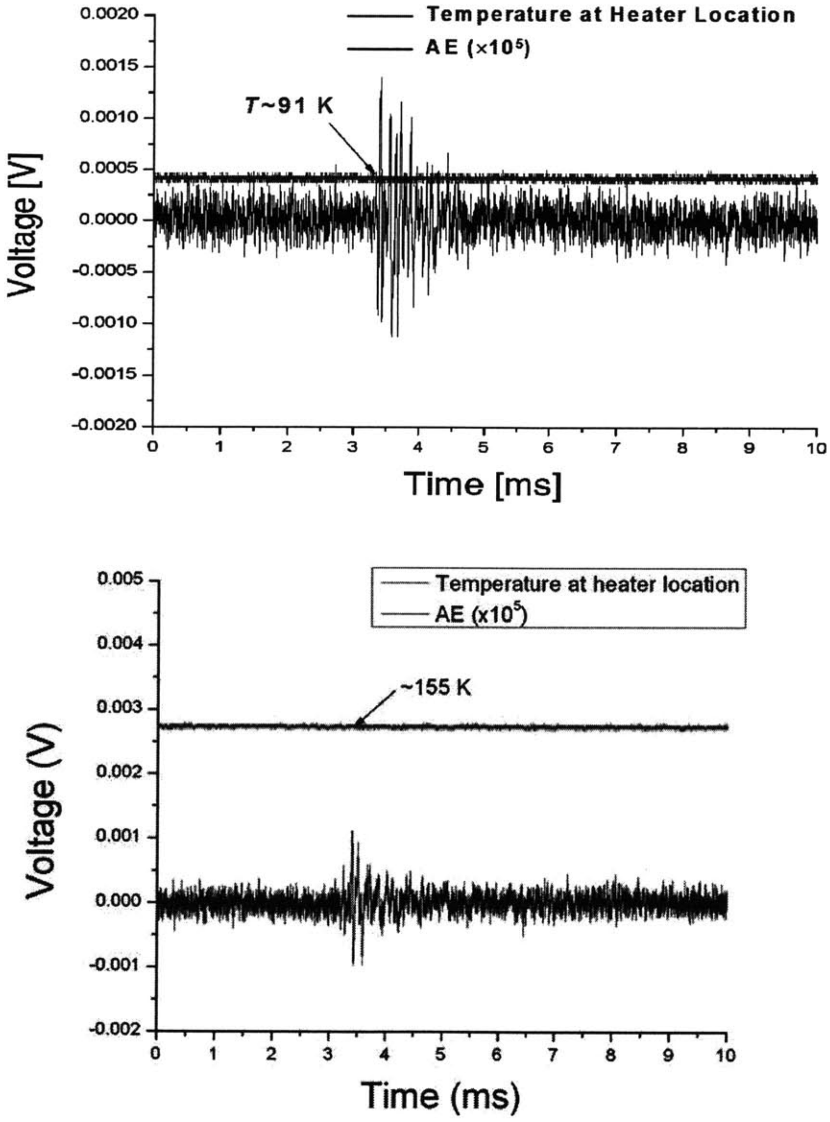

Figure 4.6.3c AE signals generated from quenching of single pancake YBCO coil without transport current

4.7 Chapter Summary

From both sets of experiments, there is evidence that AE signals can be generated during the heating of a HTS tape or a coil. The AE signals generated are caused by thermal strains induced by the time varying temperature gradients within the materials that are heated. However, the results does not conclusively indicate that AE can be used as a complement to voltage taps to detect quench events because AE signals were not observed in the pancake coil assembly until a large portion of the coil has been quenched. Also, our experiment has failed to isolate the source of the AE signal, e.g. if it was generated by the epoxy, spacer material and so forth. If the signals were generated from materials outside the tape, changing the spacer materials and so forth would affect the efficacy of AE sensing during quenching.

It appears that more work needs to be conducted to determine the source of the AE signals to determine whether AE can be used effectively to detect quenches. From 4.6 Experiment II, however, it is observed that AE is not effective in this case. For larger coil assemblies, or even in actual magnets where Lorentz forces are high, a quench event might cause significant changes in forces and cause greater slips to occur within the magnet. These events might amplify the AE waves.

In addition, since the transition from superconducting to normal does not happen as precipitously in HTS as it does in LTS, the thermal strains induced by transition might be too gradual for detection. In LTS, during a quenching process, the normal zone propagates rapidly throughout the coil, and will cause significant thermal stress differentials within the magnet. Therefore, AE detection of quenching in LTS might be a more viable idea.

Chapter 5 – Conclusion

In the previous chapters, three sub-issues of protection of HTS magnets have been explored – overheating, high voltage, and overstressing. In Chapter 2, it was shown that spacers can be designed to increase dispersion of thermal disturbances to minimize the occurrence of localized heating that can lead to permanent damage and degradation. Spacers that have the ability to do so have high thermal diffusivities, and create low contact resistances when sandwiched between tapes. It was shown experimentally that copper oxide was the promising spacer among those tested, but has its short-comings since the NZP velocity was much smaller than theoretical estimation. AC losses might also be a problem when used in a real magnet system.

In Chapter 3, the issue of internal voltage was studied for magnet systems put in persistent mode. High internal voltages are known to permanently damage magnets by voltage breakdowns within the windings. In our experiment, internal voltages were observed for a small test coil assembly and the results agree well with those of simulations. From our study, we have also discovered that the ability of a magnet to disperse thermal disturbances over large volume, as discussed in Chapter 2, also reduces the maximum internal voltage that can be generated.

Finally, to complement standard resistive voltage technique, Chapter 4 explored techniques of early quench detection using acoustic emission. A quench that results in temperature differentials within the winding should induce time-varying stresses that can be detected by an AE sensor. Our experimental results have been inconclusive as to the usefulness of AE for early detection of quench initiation because AE signals are believed to have been generated by the cracking of epoxy surrounding the test heaters.

References

[1] J. E. Jankowski, "Convective Heat Transfer Model for Determining Quench Recovery of High Temperature Superconducting YBCO in Liquid Nitrogen", *Master of Science Thesis,* MIT, 2004.

[2] Y. Iwasa, *Case Studies in Superconducting Magnets – Design and Operational Issues,* Plenum Press, New York, 1994.

[3] C.H. Edwards, D.E. Penney, *Differential Equations and Boundary Layer Problems,*Prentice Hall, NJ, 2000.

[4] H. Lee, H.M. Kim, J. Jankowski, Y. Iwasa, "Detection of 'Hot Spots' in HTS Coils and Test Samples With Acoustic Emission Signals", *IEEE Transactions on Superconductivity*, vol. 14, No. 2, June 2004

[5] Y. Iwasa, J. Minervini, MIT Course 2.64J: Superconducting Magnets - Lecture Notes, Spring Term, 2005.

[6] T. Beckwith, R.D. Marangoni, J.H. Lienhard, *Mechanical Measurements*. Addison-Wesley Publishing Company Inc., 1994.

[7] O.O. Ige, "Mechanical Disturbances in High-Performance Superconducting Dipoles", *PhD. Thesis*, MIT, 1989.

[8] M.N. Wilson, *Superconducting Magnets*, Oxford Clarendon Press, 1983.

[9] Frank P. Incropera, David P. De Witt, *Introduction to Heat Transfer*, John Wiley and Sons, New York, 1990.

[10] O.Tsukamoto, M.F.Steinhoff, and Y. Iwasa, "Acoustic Emission Triangulation of Mechanical Disturbances in Superconducting Magnets", *Proc 9th Symp. Engr/ Problems of Fusion Research,* 1981.

[11] J.W. Lue, M.J. Gouge, R.C. Duckworth, D.F. Lee, D.M. Kroeger, J.M. Pfotenhauer, "Quench Tests of a 20-cm Long RABiTS YBCO Tape", *Advances in Cryogenic Engineering,* 2002.

[12] Y. Iwasa, H. Lee, J. Fang, B. Haid, "Quench and Recovery of YBCO Tape Experimental and Simulation Results", *IEEE Transactions on Superconductivity*, vol. 13, No. 2, June 2003

[13] R. Bellis, Y. Iwasa, "Quench Propagation in High T_c Superconductors", *Cryogenics*, vol. 34, No. 2, 1994

[14] Y. Iwasa, "Stability and Protection of Superconducting Magnets – A Discussion", *ASC Conference,* 2004

[15] T. Ishigohka, O. Tsukamoto, Y. Iwasa, "Method to Detect a Temperature Rise in Superconducting Coils with Piezoelectric Sensors", *Applied Physical Letters* **43** (3), 1983

[16] H. Maeda, O. Tsukamoto, Y. Iwasa, " The Mechanism of Frictional Motion and its effects at 4.2 K in Superconducting Magnet Winding Models", *Cryogenics,* June 1982

[17] Y. Iwasa, *HTS Magnet: Stability and Quench Protection – An Overview*, Quench Workshop, FL, January 2005

[18] D. Hanselman, B. Littlefield, *Mastering MATLAB®,* Prentice Hall, NJ, 1996

Appendix – Simulation Codes

This is the Matlab® code used to simulate the internal voltage experiment in Chapter 3.

```
clear all;

%for small test assembly, L=690 micro, k=0.51, Rj=210E-6

Dt=0.05; %Time Step
NumTimeStep=120; %Number of time steps to be run
L=1; %m
Tcs=84;
Tc=90;
I_o=40;
I_to=I_o;
Vc=1E-9; %in micro-volt/m
L1=690E-6; %Henry
L2=690E-6 ;
k=0.51;
M12=k*(L1*L2)^0.5;
n=15; %tape index number
Icrit=42;
m=2;
Rj=0; %joint resistance

%Resistance of the matrix
p_cu=3E-9; % in m
p_ni=5.7E-9; % ohm-m
A_cu=100E-6*4E-3;
A_ni=75E-6*4E-3; %Change Later

Rm=(p_cu*p_ni*L)/(p_ni*A_cu+p_cu*A_ni);

%%%%%%%%%%%%%%%%%%%%%%%%%%%%%%%%%

%Creating Arrays to store values

t=zeros(NumTimeStep,1);
T=zeros(NumTimeStep,1);
Is=zeros(NumTimeStep,1);
Im=zeros(NumTimeStep,1);
It=zeros(NumTimeStep,1);
IcM=zeros(NumTimeStep,1);
Reff=zeros(NumTimeStep,1);
RsM=zeros(NumTimeStep,1);
V21=zeros(NumTimeStep,1);
V10=zeros(NumTimeStep,1);
Vresis=zeros(NumTimeStep,1);
Vind=zeros(NumTimeStep,1);

%Value for temperature Simulation

h=80;
w=170E-6;
tk=4E-3; % thickness of tape
```

```
Q=6; %power input [W]
Cp=8900*220;
To=77.3;

%Voltage simulation
Reff(1)=0;
Is(1)=I_o;
It(1)=I_o;

for t1=Dt:Dt:Dt*(NumTimeStep)
  T1=(Q/(2*h*L*w))*(1-exp(-(2*h/(tk*Cp))*t1))+To;
  t(m)=t1;
  T(m)=T1;

  kk=1/Tc;
  Ic=Icrit./(1+exp((T(m)-Tcs)/(kk*Tc)));

  if (Ic<0)
    Ic=0;
  end

  %Algorithm to solve for current in superconductor

  for (It1=It(m-1):-0.01:(It(m-1)-0.01*200))

    if (Ic>0)
      c8=(Vc*L)/(Ic^n);
    else c8=(Vc*L)
    end

      b8=Rm;
      a8=It1;

      x1=0;
      x2=Is(m-1);

      for i=1:100
        y1=c8*x1^n+b8*x1-a8*b8;
        y2=c8*x2^n+b8*x2-a8*b8;

        if (y1*y2<0)
          x1_t=(x1+x2)/2;
          x2_t=x2;
          y1_t=c8*x1_t^n+b8*x1_t-a8*b8;
          y2_t=c8*x2_t^n+b8*x2_t-a8*b8;
          if (y1_t*y2_t<0)
            x1=x1_t;
            x2=x2_t;
          else
            x1=x1;
            x2=(x1+x2)/2;
          end
        end

        if (abs(x1-x2)<=1E-6)
          Is1=x1;
          break
        end
```

```
        end

        if ((It1-Is1)*Rm+Rj*It1+(L1+L2+2*M12)*((It1-It(m-1))/Dt)<=1E-6)
          break
        end
   end


   %Storing data in arrays

   It(m)=It1;
   Is(m)=Is1;
   Im(m)=(It1-Is1);
   IcM(m)=Ic;

   if (Ic>1e-2)
      Rs=(Vc*L/Ic)*(Is1/Ic)^(n-1);
   else
      Rs=0;
   end

   RsM(m)=Rs;
   Reff(m)=(Rm*Rs)/(Rm+Rs);

   V21(m)=-(L2+M12)*((It1-I_to)/Dt)-(It1*(Reff(m)+Rj));
   Vresis(m)=It1*Reff(m);
   Vind(m)=-(L1+L2+2*M12)*((It1-I_to)/Dt);
   V10(m)=-(L1+M12)*((It1-I_to)/Dt);
   I_to=It1;
   m=m+1;
end

%This part takes in user input to overlay experimental results

ActVolt=importdata('40A-profile.txt');
time=ActVolt(:,1)-6;
V84=ActVolt(:,2);
V40=ActVolt(:,3);
V87=ActVolt(:,4);

%Plotting graphs
figure(4);
[h1]=plot(t((2:m-1),1),T((2:m-1),1))%t((2:m-1),1),IcM((2:m-1),1))
set(h1,'LineWidth',1.5);
xlabel('Time [s]')
ylabel('Temperature [K]')
title ('Simulated Temperature in Heated Length')

figure(1);
[h2]=plot (t((2:m-1),1),V21((2:m-1),1)*1000, t((2:m-1),1),V10((2:m-1),1)*1000)
set(h2,'LineWidth',1.5);
legend('Sim: V84','Exp: V84','Sim: V40','Exp: V40')
xlabel('Time [s]')
ylabel('Voltage [mV]')
title('Comparison between Experimental and Simulated Voltages')

figure(2);
```

```
[h3]=plot(t((2:m-1),1),Reff((2:m-1),1)*1000,t((2:m-1),1),RsM((2:m-1),1)*1000,t((2:m-1),1),Rm*(IcM((2:m-
1),1)./IcM((2:m-1),1))*1000)
set(h3,'LineWidth',1.5);
xlabel('Time [s]')
ylabel('Resistance [m-Ohm]')
legend('Reff','Rs','Rm')
title('Simulated Resistances')

figure(3);
[h4]=plot (t((2:m-1),1),Is((2:m-1),1),t((2:m-1),1),Im((2:m-1),1),t((2:m-1),1),It((2:m-1),1))
set(h4,'LineWidth',1.5);
xlabel('Time [s]')
ylabel('Current [A]')
legend('Is','Im','It')
title('Simulated Current in Heated Length')
```